Anniken Eriksrud Karlsen

Traveling Wave Fault Location on HVDC-MMC Transmission Lines

Master's thesis in Energy and Environmental Engineering
Supervisor: Hans Kristian Høidalen
June 2023

NTNU
Norwegian University of
Science and Technology

Anniken Eriksrud Karlsen

Traveling Wave Fault Location on HVDC-MMC Transmission Lines

Master's thesis in Energy and Environmental Engineering
Supervisor: Hans Kristian Høidalen
June 2023

Norwegian University of Science and Technology
Faculty of Information Technology and Electrical Engineering
Department of Electric Power Engineering

NTNU
Norwegian University of
Science and Technology

Preface

This master's thesis has been conducted at the Department of Electric Energy at the Norwegian University of Science and Technology (NTNU) in the period from January 2023 to June 2023.

First of all, I would like to thank my main supervisor Hans Kristian Høidalen for good guidance and professional support throughout the specialization project and the master's thesis. This has been important when choosing which direction this thesis should take. I would also like to thank my co-supervisors Anders Elvebakk from Statnett and Ph.D. candidate Thomas Treider for support when I have had questions.

Working with the PSCAD model, I obtained information for the overhead line and sub-sea cable models from Statnett for the specialization project. This data has further been used in the thesis. I would therefore like to thank Bjarni Helgi Thorsteinsson and Gunnar Evenset for providing me with transmission line data for the model. Also, a thank you to Raymundo Torres for helping me in making the PSCAD model work.

I would like to thank my fellow students at the High Voltage Technology (HVT) research group for a good working environment both academically and socially. Lastly, a big thanks to Ph.D. candidate Fanny Skirbekk for being a good role model for several years and for contributing with motivation and support during the thesis.

25/06/2023, Trondheim

Anniken Eriksrud Karlsen

Abstract

With an increasing need for electric energy, high voltage direct current (HVDC) systems have become more popular. These systems have several advantages compared to high voltage alternating current (HVAC) systems, being able to transfer more power with minimal losses. Traveling wave protection is a suitable choice for HVDC lines, which also gives the possibility of utilizing traveling wave fault location (TWFL). In this thesis, a TWFL algorithm has been developed to investigate the fault location of HVDC faults and power system incidents occurring in the HVDC system. An HVDC system with modular multilevel converters (MMC) has been modeled using the PSCAD software. This model is a hybrid transmission line based on the NordLink interconnector. Faults such as pole-to-ground faults and lightning strikes have been applied on the overhead line. AC grid disconnection has also been simulated. Lastly, a DC voltage source model has been developed and pole-to-ground faults were applied, to compare this model to the original HVDC-MMC model.

Single-ended and double-ended TWFL algorithms were developed, utilizing discrete wavelet transformation (DWT) for signal processing. The fault location was based on the location of the detail coefficient peaks on one or both terminals, dependent on whether the single-ended or double-ended method was used. The accuracy of the fault location results was dependent on the different simulation cases. With varying fault positions and fault resistances, the algorithms mostly located the faults within reasonable errors. However, a fault resistance of $100\,\Omega$ caused fault location failure for both algorithms. The responses were more damped, causing the detail coefficient peaks to be low. When applying lightning strikes of different current amplitudes on the overhead line, the incoming waves resulted in both a positive and a negative detail coefficient peak. This resulted in fault location failures for the single-ended algorithm. The double-ended algorithm located the faults correctly. AC grid disconnection did not give fault location.

Lastly, the MMC model was compared to the DC voltage source model to investigate if it is possible to obtain the same fault response and reduce the computational load of the simulation. The fault location results were not affected by using this simplified model. The detail coefficients were slightly changed, but the peaks appeared at the same locations in time. By using a smaller time step of $1\,\mu$s in the DC source model, the fault location results were not as good compared to the sampling time of $2\,\mu$s.

Sammendrag

Med et økende behov for elektrisk energi, har høyspentsystemer med likestrøm (HVDC) blitt mer populært. Disse systemene har flere fordeler sammenlignet med høyspentsystemer basert på vekselstrøm (HVAC), blant annet ved at de kan transportere mer energi med minimalt tap. Vandrebølgevern er et godt valg for HVDC-systemer. Dette gir også muligheter for bruk av feillokalisering ved hjelp av vandrebølger (TWFL). I denne oppgaven er det utviklet feillokaliseringsalgoritmer basert på vandrebølger for bruk på HVDC-feil og andre netthendelser. Et HVDC-system bestående av modulære flernivå-omformere (MMC) er modellert i PSCAD. Denne modellen er en hybrid transmisjonslinje basert på NordLink-forbindelsen. Fase-jord-feil og lynnedslag har blitt påført på luftledningen. Utkobling av nærliggende AC-nett har også blitt simulert. Til slutt har en enkel DC-modell blitt laget og fase-jord-feil har blitt simulert for å sammenligne denne modellen med den originale HVDC-MMC-modellen.

Ensidige og tosidige TWFL-algoritmer har blitt utviklet, hvor diskret wavelettransformasjon (DWT) har blitt brukt for signalbehandling. Feillokaliseringen baserte seg på analyse av topp- og bunnpunktene til detaljkoeffisientene. Antall måleterminaler brukt var avhengig av om ensidig og tosidig feillokalisering ble brukt. Nøyaktigheten til feillokaliseringen varierte med de ulike simuleringstilfellene. Med varierende feilposisjoner og feilmotstander, klarte algoritmene i de fleste tilfeller å lokalisere feilstedet med en liten feilmargin. For en feilmostand på $100\,\Omega$ derimot, klarte ikke algoritmene å lokalisere feilen i alle tilfeller. Responsene var dempet, som forårsaket at detaljkoeffisientene var små. Ved å teste lynnedslag for forskjellige lynamplituder på luftledningen ga alle vandrebølgene både et toppunkt og et bunnpunkt i detaljkoeffisientene. Dette resulterte i at den ensidige TWFL-algoritmen feilet. Den tosidige algoritmen klarte å lokalisere alle feil. Utkobling av nærliggende AC-nett ga ingen feillokalisering.

Til slutt ble MMC-modellen sammenlignet med en forenklet DC-modell for å se om det er mulig å oppnå samme feilrespons og redusere simuleringsbelastningen. Resultatene av feillokaliseringen ble ikke påvirket av å bruke den forenklede modellen. Detaljkoeffisientene endret seg noe i verdi, men lokasjonen til bølgene i tidsaksen var like. Ved å bruke et mindre tidsskritt på $1\,\mu s$ for DC-modellen, ble ikke feillokaliseringen like god sammenlignet med å bruke et tidsskritt på $2\,\mu s$.

Table of Contents

List of Figures

List of Tables

Abbreviations

AC alternating current

CB circuit breaker

CCSC circulating current suppression control

CWT continuous wavelet transform

DC direct current

DWT discrete wavelet transform

EMTDC Electromagnetic Transients including DC

HVAC high voltage alternating current

HVDC high voltage direct current

IGBT Insulated-Gate Bipolar Transistor

LCC Line Commutated Converter

MMC Modular Multilevel Converter

PSCAD Power Systems Computer Aided Design

PWM pulse width modulation

TSO Transmission System Operator

TW traveling wave

TWFL traveling wave fault location

VSC Voltage Source Converter

Chapter 1

Introduction

1.1 Background

The need for electric energy is increasing, making high voltage direct current (HVDC) systems more popular. These systems have several advantages compared to the conventional high voltage alternating current (HVAC) transmission systems. HVDC systems have the ability to connect asynchronous systems, which is not possible with pure HVAC systems. These systems are also able to transmit power over long distances with minimum losses, making HVDC an optimal choice. There are several HVDC transmission systems in Norway, connecting Norway to other countries in Europe. Some examples are the North Sea Link, NordLink, and NorNed [1], [2]. The NordLink interconnector stands out as the only hybrid HVDC transmission line in Norway. It consists of an overhead line directly connected to a sub-sea cable transporting power energy between Norway and Germany. On the German side, a land cable is used [1]. The NordLink interconnector is based on the use of Modular Multilevel Converter (MMC) technology. MMCs are commonly used in HVDC systems to convert between alternating current (AC) and direct current (DC) and have several advantages compared to previous converter technologies [3]. Hybrid HVDC transmission lines are more difficult to protect as the lines can be subjected to many different fault conditions. This gives new challenges regarding protection systems, as overhead lines are more subject to faults than underground and sub-sea cables. There have been few studies regarding fault location on hybrid Voltage Source Converter (VSC) transmission system consisting of overhead lines and cables, thus making it an interesting case [4].

Protection systems for transmission lines are essential for maintaining stable and reliable power operation. Traveling wave protection is confirmed to be a suitable choice for HVDC lines [5]. This method is based on the traveling wave (TW) generated by a fault and is the fastest method for fault detection. It also gives the possibility of fault location, which is important for minimizing possible reparation time and overall costs of permanent faults. A study conducted about fault location on an HVDC transmission line in Brazil concludes that traveling wave fault location (TWFL) gives significantly better accuracy compared to impedance-based fault location methods [5].

1.2   Problem description

The thesis is a continuation of a specialization project delivered in December 2022 [6]. This project gave a general overview of what types of fault detection and location methods are commonly used on HVDC transmission lines. A simplified DC grid model of a hybrid transmission line was developed, with the transmission line data based on the NordLink interconnector.

With this work as an introduction to protection systems, the master thesis will go more in-depth on using traveling waves for fault location on HVDC-MMC transmission lines. The purpose of the thesis is given below:

- Develop an HVDC-MMC model in PSCAD based on the NordLink interconnector and run simulations on HVDC overhead line faults and other power system incidents.

- Develop a TWFL algorithm using wavelet transformation in MATLAB for double-ended and single-ended fault location.

- Investigate how the TWFL accuracy is influenced by different system parameters and modeling approaches, and compare the proposed TWFL algorithms.

1.3   Preliminary work

The following sections in this thesis are taken from the specialization work with some improvements for better readability [6]:

Chapter 2.4.3: DC circuit breakers and fault clearance

Chapter 3-3.1: Traveling wave detection and fault location, in addition to the first paragraph of 3.1: Traveling waves

Chapter 4.1-4.1.1: PSCAD modeling

1.4   Structure of thesis

The thesis is structured the following way: Chapter 2 gives a theoretical foundation of HVDC-MMC systems, DC faults, and fault clearance strategies. Chapter 3 introduces the principles for detecting traveling waves and the TWFL concepts. Chapter 4 explains the implementation of the PSCAD HVDC-MMC model and the proposed MATLAB TWFL algorithms. Decisions that have been made are justified. Chapter 5 gives the fault location results with short comments on fault location failures. Lastly, chapter 6 discusses factors influencing fault location accuracy with a comparison of the TWFL algorithms. An appendix is provided at the end of the thesis with necessary information when this is needed.

Chapter 2

HVDC-MMC systems

This chapter provides a brief introduction to the motivation behind the use of MMCs and why this is an attractive choice when developing new HVDC systems. The principles of MMCs are investigated, exploring the modulation techniques, control strategies, and fault-handling capabilities. The most common DC faults are also explained.

2.1 Motivation behind the development of MMCs

Converters are essential in the control of HVDC grids [7]. Thus, converter technologies have been developed over several years resulting in the common use of modular converters today, such as the MMC. Line Commutated Converter (LCC) was the first converter technology to be developed, first utilizing mercury arc valves before thyristors were implemented in 1967 [8]. LCC technology is frequently used today and is called the "classical HVDC" [9]. In Norway, the NorNed interconnector is based on the use of LCC [2].

Due to the drawbacks of using LCC technology in HVDC systems, VSC technology has been developed. This technology was first introduced around 1990, based on the use of Insulated-Gate Bipolar Transistor (IGBT) instead of thyristors [10, p. 16]. IGBTs have the advantage of turn-on and turn-off capabilities. This means that they are fully controllable by using gate signals to turn the transistors on and off. Another reason to use VSC is that LCC technology is highly dependent on the AC grid. Therefore black starts are not possible utilizing LCC [11]. For VSC systems, a black start can be achieved as VSCs can generate voltage from the stored energy in the converter capacitors [12]. Black start capability is important to secure a stable power system during power outages, as VSC systems can feed voltage into the AC grid that has a power outage. A grid based on LCC technology, however, will be affected by a power outage in the AC grid as it cannot generate voltage on its own.

With the VSC system, a more accurate grid control can be achieved [11]. Being able to control both active and reactive power, VSC systems can adjust the power system quantities and ensure the reliable operation of the system.

Thus, the requirement of using filters is higher for LCC systems than for VSC systems. During recent years, VSC technology has been further developed from using two-level converters with poor harmonic distortion to multilevel converters [11]. With multilevel converters, the generation of harmonics is reduced significantly. By using a high amount of voltage levels, the voltage response is closer to the reference signal [13]. The quality of the output voltage is therefore also higher due to reduced harmonics.

The advantages of multilevel converters compared to other converter technologies have contributed to making the MMC technology the preferred converter technology in HVDC-VSC projects worldwide [3], [14].

2.2   MMC topology and control principles

An MMC can operate as a rectifier or inverter depending on the current flow. Figure 2.1 shows the topology of an MMC operating in rectifier mode [15]. The MMC is structured with each incoming AC phase connected to an upper and lower converter arm, each arm working as a controllable voltage source. The six converter arms consist of arm reactors connected in series with individually controllable submodules. Arm reactors limit current harmonics generated from faults, and this way reduce the fault currents [3], [16]. They also compensate for the voltage differences between the upper and lower arms of each leg [17], [18].
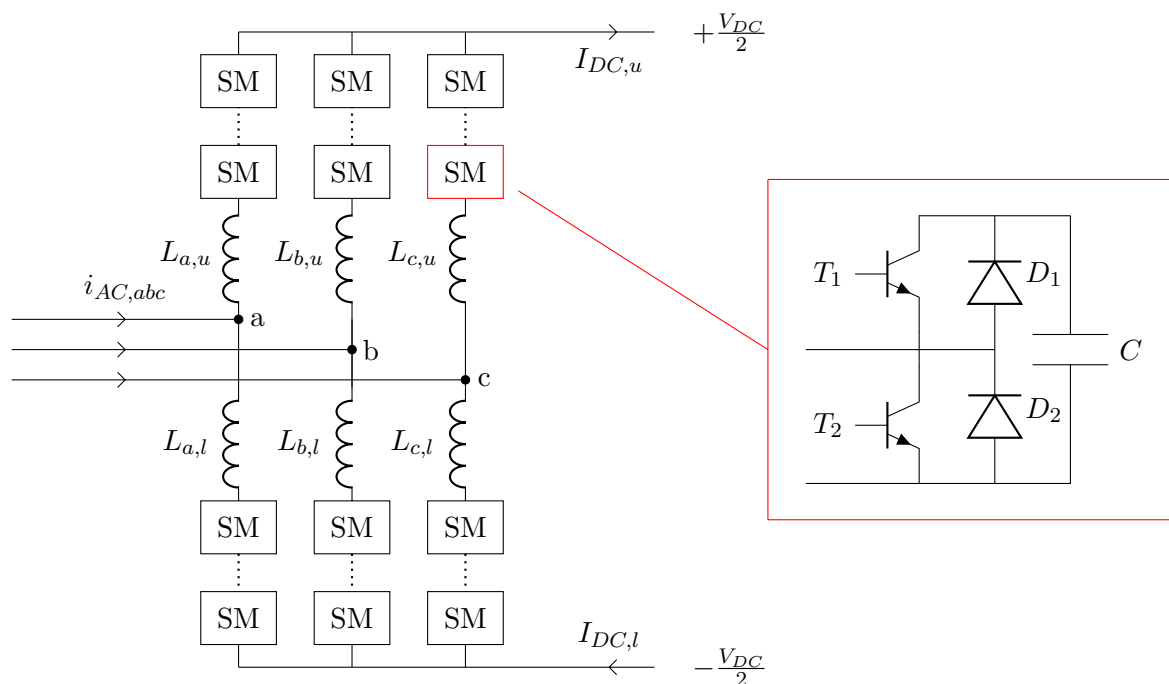
Figure 2.1: Half-bridge MMC structure

The figure shows a structure with half-bridge submodules, which is a commonly used today [19]. Two IGBTs and two diodes are connected in anti-parallel, with a capacitor working as an energy storage [16]. The IGBTs only conduct current in one direction illustrated in the figure.

This way, it is possible to control the current path by turning the IGBTs on and off.

In the figure above, u denotes the upper arms of the rectifier, while l denotes the lower arms. The equations for the upper and lower DC currents are formulated using Kirchhoff's current law, given in (2.1) and (2.2). $\{a, b, c\}$ correspond to each leg, which also corresponds to each of the AC phases.

$$I_{DC,u} = i_{a,u} + i_{b,u} + i_{c,u} \tag{2.1}$$

$$I_{DC,l} = i_{a,l} + i_{b,l} + i_{c,l} \tag{2.2}$$

The input AC current can be formulated as given in (2.3) where $i = \{a, b, c\}$.

$$i_{AC,i} = i_{i,u} - i_{i,l} \tag{2.3}$$

The DC output voltage of the MMC rectifier is dependent on several factors. Some of these are given below:

- Modulation index: The modulation index is described by the following formula [20]:

$$M = \frac{2V_{AC}}{V_{DC}} \tag{2.4}$$

   where V_{DC} is the pole-to-pole DC voltage. This index describes the ratio between the AC and DC voltage.

- Arm reactor: Simulations show that an increasing inductance leads to a damped fault current. The relationship between these parameters is given in (2.5) [21].

$$L_{arm} = \frac{V_{DC}}{2\alpha} \tag{2.5}$$

   where α is the fault current rise rate in $[\frac{kA}{s}]$.

- Submodule capacitance: The voltage over each submodule capacitor will vary during converter operation due to module switching. The voltage ripple is dependent on the capacitance value [22].

- Number of submodules (N): A large number of submodules gives a larger amount of voltage levels. This is given in (2.6) where V_{SM} is the voltage of one submodule.

$$V_{DC} = N \cdot V_{SM} \tag{2.6}$$

Kirchhoff's voltage law is used to formulate the correlation between the input AC voltage and the output DC voltage in each arm. For the upper part of the converter, this is given in (2.7). $L_{i,u}\frac{di_{L_{i,u}}}{dt}$ is the voltage over the arm reactor. $R_{i,u}i_{i,u}$ is the loss occurring in each upper leg.

$$\frac{V_{DC}}{2} = v_{AC,i} + L_{i,u}\frac{di_{L_{i,u}}}{dt} + R_{i,u}i_{i,u} + V_{SM,tot,u} \tag{2.7}$$

2.2.1   Submodule operation modes

MMCs can consist of many submodules in each arm. The submodules can operate in three different modes, these are given in Table 2.1 [16]. Each of these modes has two states, dependent on the direction of the current flow. The first mode is the on-state with T1 on and T2 off [23]. T1 and T2 correspond to the IGBTs in Figure 2.1, and C is the capacitor bank of the submodule. In off-state, T1 is off and T2 is on. The capacitor charge remains constant in this mode. In block-state, both IGBTs are off and the change in capacitor charge depends on the current flow direction.

Table 2.1: Submodule operation modes

Mode	T_1	T_2	C
On-state	On	Off	Charged/discharged
Off-state	Off	On	Constant
Block-state	Off	Off	Charged/constant

The path of the current through the submodule is dependent on the operation mode and the current flow. Figure 2.2 gives the different modes with positive current flow. In on-state, the current will not flow through the lower part of the submodule because T2 is off. As T1 cannot pass a current in the positive direction, the current flows through the diode D1 instead, and further through the capacitor. This increases the capacitor voltage, thus the capacitor is charged. In off-state, T2 is passing the current, and the capacitor is not involved. In block-state, the current can only pass through the diodes. In this case, this is D1. This gives the same current path as in on-state and the capacitor is charged.

On-state   **Off-state**   **Block-state**
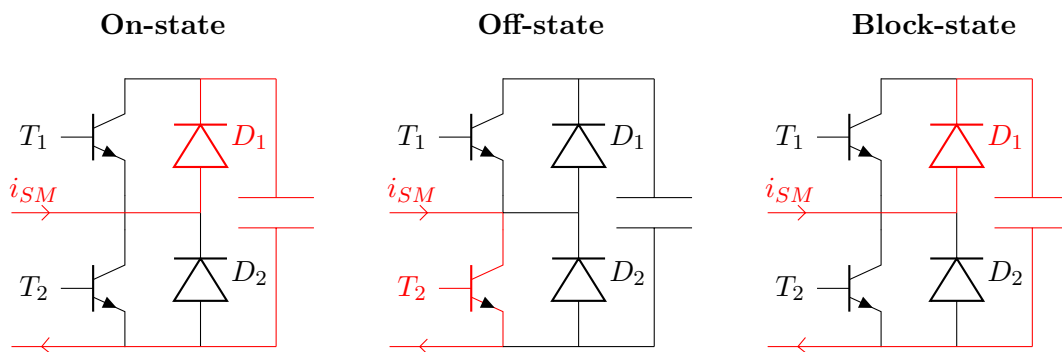
Figure 2.2: Operation modes of half-bridge submodules with positive current flow

When changing the current direction to a negative current flow, the on-state current now flows through T1, and the capacitor is discharged. This is shown in Figure 2.3. In off-state, the negative current flows through the diode D2, as it cannot pass through T2 because of the direction of the IGBT. In block-state, the current is similar to the current on the off-state, flowing through D2 and the capacitor charge is not affected.

On-state   **Off-state**   **Block-state**
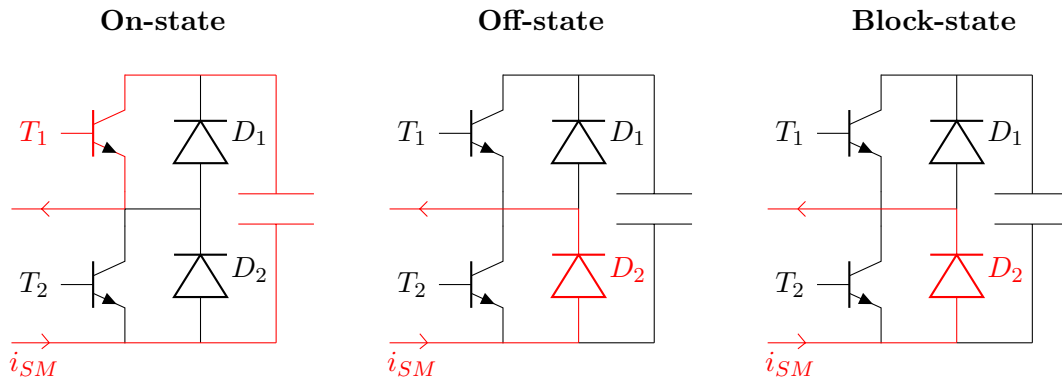
Figure 2.3: Operation modes of half-bridge submodules with negative current flow

Because of the high amount of submodules in the MMC, there are large numbers of submodule mode changes during operation. This contributes to rapid changes in capacitor voltages. The number of submodules in on-state and off-state is dependent on the reference voltage. Control systems are therefore important to secure that the MMC is operating in a reliable way and does not contribute to very high currents flowing in the converter.

2.2.2 MMC control

For a radial HVDC transmission system with one transmission line, there are two MMCs. One operates as a rectifier and the other as an inverter, making them able to operate in different control modes. There are four possible control modes, these are given below [17]:

- DC voltage control mode

- DC current control mode

- Active power control mode

- AC voltage control mode or reactive power control mode

The control functions of the HVDC-MMC system can be divided into two main groups, shown in Figure 2.4 and is based on [24]. The VSC control, or upper level control, is a general control suited for the conventional 2-level VSC [24]. This part utilizes the control modes mentioned above, such as DC voltage and active power control, to keep these general system parameters within their limits of operation. The VSC control contains an outer and inner controller shown in the figure.
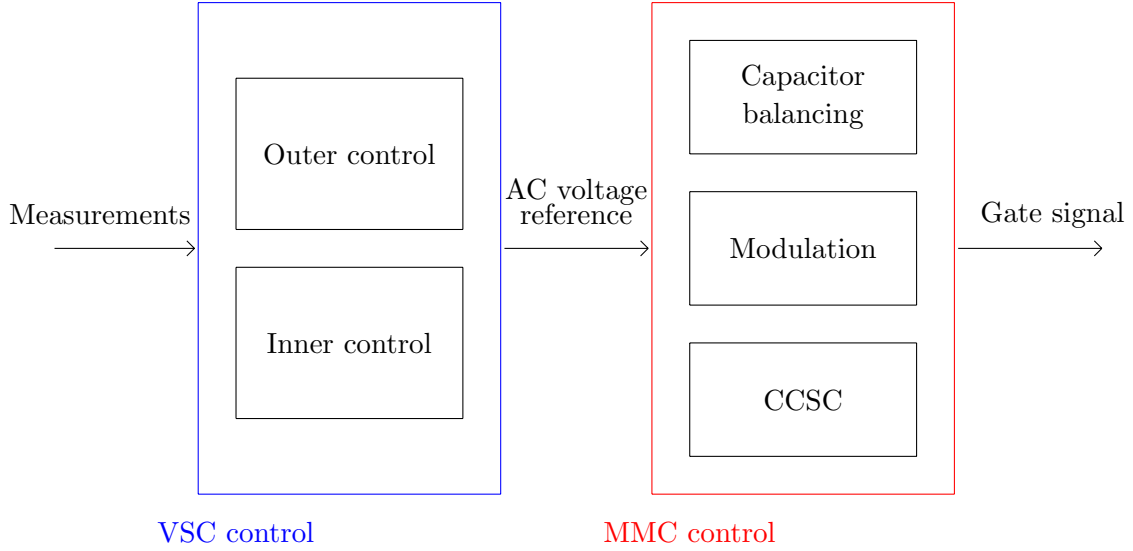
Figure 2.4: Overview of control functions for the MMC

As the MMC has more complex features than the 2-level VSC, MMC control, also called lower level control, is necessary [25]. The figure shows the most important control mechanisms. These are circulating current suppression control (CCSC), modulation, and capacitor voltage balancing.

A common control strategy for VSC control is the vector control strategy. This strategy is based on the dq-decoupling [17], [26], [27]. The dq-frame stands for the direct-quadrature framework and is used for easier control of active and reactive power [27]. The transformation between the ABC-frame and the dq-frame can be done directly by using the Park transformation given in (2.8) [28].

$$X_{dq0} = \frac{2}{3} \begin{bmatrix} \cos\theta & \cos\theta - \frac{2\pi}{3} & \cos\theta + \frac{2\pi}{3} \\ -\sin\theta & -\sin\theta - \frac{2\pi}{3} & -\sin\theta + \frac{2\pi}{3} \\ \frac{1}{2} & \frac{1}{2} & \frac{1}{2} \end{bmatrix} X_{abc} \tag{2.8}$$

CCSC

Due to rapid submodule mode switching, the capacitor voltages vary. Thus, circulating currents will flow between the phase legs [15]. These currents can contribute to higher losses in the converter and can result in converter faults if the currents get large enough. To prevent these consequences, CCSC is utilized.

The circulating currents occurring in each phase can be defined. (2.9) and (2.10) gives the currents for the upper and lower arms for phase a [29]. i_{circ} is the circulating current.

$$i_{a,u} = i_{circ} + \frac{i_a}{2} \tag{2.9}$$

$$i_{a,l} = i_{circ} - \frac{i_a}{2} \tag{2.10}$$

CCSC reduces the AC component of the circulating current, which contributes to reducing the second-order harmonic components that are generated from circulating currents [30].

Modulation techniques

There exist several types of modulation techniques commonly used for MMCs, such as the pulse width modulation (PWM). PWM is a technique where pulses are generated and used as a modulation signal. The main goal of this method is to reduce the voltage harmonics and boost the voltage magnitude [19]. For MMCs, multicarrier PWM techniques are used. This means that several carrier waveforms are applied. These multicarrier waveforms can be phase-shifted and level-shifted [31]. The general phase-shifted technique uses phase-shifted carrier waveforms, but the amplitudes and shapes are the same. The level-shifted technique uses carrier waveforms at different voltage levels but the phase is the same.

Another modulation technique commonly used is the nearest level modulation technique, also called nearest level control [17], [24]. This technique determines the number of submodules in on-state at each time instant to follow the reference voltage properly. (2.11) determines the number of inserted submodules, meaning submodules in on-state [17].

$$n_{nl} = round(\frac{v_{ref}}{V_c}) \tag{2.11}$$

v_{ref} is the voltage reference and V_c is the capacitor voltage of one submodule. By rounding the final value to the nearest integer, the converter knows how many submodules need to be switched on to follow the reference voltage.

Capacitor voltage balancing

Capacitor voltage balancing is one of the main challenges when using HVDC-MMC systems [32]. The purpose is to equally distribute the capacitor voltages in each converter arm.

When determining which submodules should be switched on and off the following method can be used [15], [17]: For a positive current flow, the submodule in on-state will charge the capacitor further. Considering this, the best choice is to switch the submodule with the highest charge off and the module with the lowest charge on. This is to secure that the voltage differences are set to a minimum level. For a negative current flow, however, the strategy is the opposite as the current will discharge the capacitor. Thus, the submodule with the highest charge is set in on-state and the module with the lowest charge is bypassed.

2.3   System configurations

A radial HVDC system can have different configurations. The two most common system configurations are monopolar and bipolar. Monopolar systems use two converters and one transmission line for HVDC power transmission, as seen on the left side in Figure 2.5. The return path of this system can vary depending on the system requirements and the overall costs of implementing it. It is possible to use a conductor similar to the transmission line conductor, this makes the system symmetric. Other solutions are using metallic wires or the ground as return paths [33]. Ground return can be achieved by using sea-water for sub-sea transmission lines, or using the earth [34]. The polarity of monopolar systems is often negative because this reduces the corona impact compared to using a positive polarity [33]. The other typical power system configuration is the bipolar system. This system has double amount of converters on each terminal and two transmission lines. The MMCs on the same terminal have the same control principles as they operate in the same mode. The bipolar configuration is shown to the right in Figure 2.5. The conductors are balanced when operating under normal conditions, where one conductor has a positive polarity and the other a negative polarity [35].
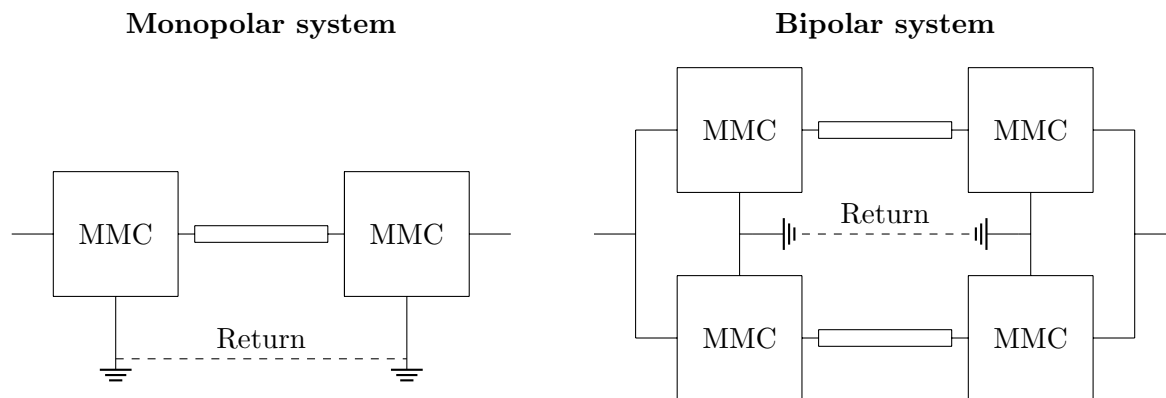
Figure 2.5: Monopolar and bipolar system configurations with return paths

When developing new transmission systems, the choice of system configuration is dependent on several factors such as cost, redundancy, necessary transmission capacity, and environmental requirements [27]. Monopolar systems have no redundancy, meaning that a fault on the transmission line will lead to an unavailable system [36]. However, the costs of monopolar systems are lower compared to implementing bipolar systems. To fulfill the N-1 criterion, the bipolar system needs to have a metallic return [27]. This criterion says that the system needs to be capable of still utilizing its purpose when a fault occurs. The metallic return can therefore replace the faulty conductor, to maintain the same power transfer capability. Bipolar configurations with ground returns are able to work as monopolar systems in case of faults on one of the poles, they do therefore have some redundancy [27].

2.4 HVDC overhead line faults and fault clearance

All parts of an HVDC system can be subject to faults. This includes the HVDC grid, the power electronic equipment such as converters, and the HVAC grid connected to the converters. Faults occurring on the DC side give large inrush currents because of the system capacitor charges [37]. HVDC transmission lines can consist of overhead lines combined with cables, subsea and underground. Compared to overhead lines, cables are highly capacitive, thus having a higher stored current charge [38]. With this energy, the cable can compensate for voltage changes. Overhead lines, on the other hand, are more inductive. Inductive components have the opposite abilities by compensating for sudden current changes in a system.

Faults can be either temporal or permanent. Temporal faults mostly occur on overhead lines, due to the lines being subject to different weather conditions. Such conditions can be wind conditions, snow and ice, and small lightning strikes. These types of faults do not cause permanent damage to the system equipment. Thus, they can be cleared and restarted shortly after fault occurrence. Permanent faults, however, require reparations and are more common in underground and sub-sea cables. The following sections will shortly describe two common faults on HVDC overhead lines, pole-to-ground faults, and lightning strikes.

2.4.1 Pole-to-ground faults

Pole-to-ground faults are the most common type of fault occurring on HVDC transmission lines, and happen if one of the poles becomes grounded [39]. Such grounding can occur on overhead lines and cables for various reasons. Some examples are conductors getting in contact with ground wires or trees, icing, or faults caused by cable isolation damage. This type of fault leads to a large fault current, which may damage the power equipment if the fault is not detected and cleared fast enough. An example of the pole response of a single pole-to-ground fault is shown in Figure 2.6. These responses have been obtained by Muniappan (2021) [40]. The DC voltage at the positive pole quickly decreases to zero, while the DC current increases rapidly before it at a specific point starts decreasing. Muniappan states that the responses depend on fault location and fault resistance.

(a) DC voltage response   (b) DC current response
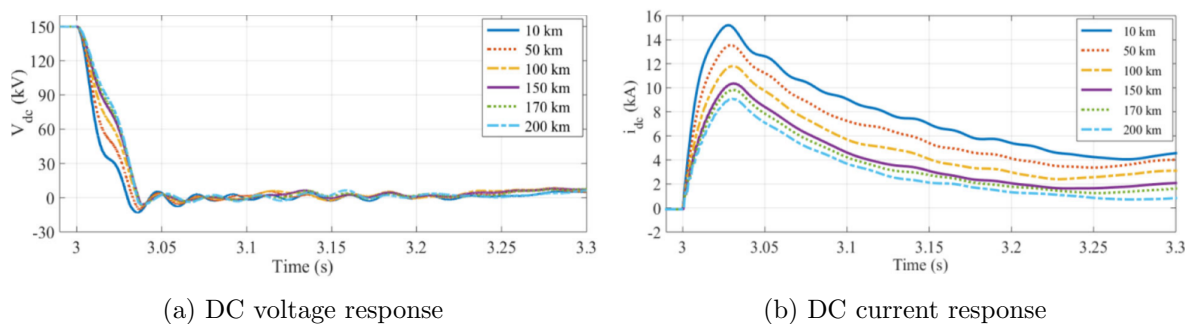
Figure 2.6: HVDC-VSC faulty pole response of a positive pole-to-ground fault [40]

2.4.2 Lightning strikes

Lightning strikes are caused by electrical charges in the atmosphere and can be dangerous both to humans and electrical equipment. This phenomenon happens regularly on overhead transmission lines, either directly or indirectly [41], [42]. A direct lightning strike hits the transmission line construction, where the consequences depend on the lightning strike location and amplitude. As seen in Figure 2.7, the HVDC overhead line usually consists of line conductors with opposite polarities (C1 and C2) and one or several ground wires (GW) located on a higher level. Direct strikes usually occur on the ground wire. As a lightning strike finds the shortest way to the ground, ground wires are placed on a higher level than the conductors, as a protection. This way, a large part of the lightning current will go through the ground wire, via the tower constructions, and to the ground, while a smaller part flows through the conductor [43]. However, if a shielding failure occurs, the lightning strike will hit the conductors directly [42], [44]. However, this type is considered to be rare [44]. Indirect lightning strikes give smaller consequences, as these first hits another object or the ground before some of it goes into the transmission line.
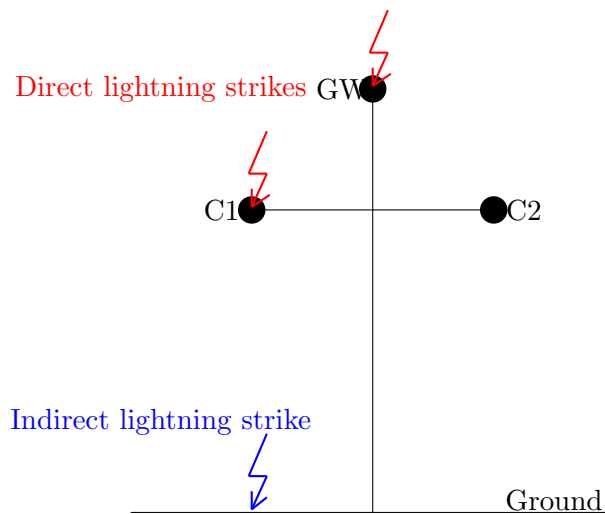
Figure 2.7: Types of lightning strikes on an overhead line

Lightning strikes can cause temporal or permanent faults, depending on whether the power equipment is able to withstand the over-voltages and over-currents occurring. Permanent faults may lead to high reparation costs and power system downtime. According to Hoidalen (2022) [43] is 3 kA the lowest lightning current amplitude that can occur, and amplitudes up to 200-300kA have been measured. Cables can also be vulnerable to lightning strikes in hybrid transmission lines. This is because a strike on the overhead line can cause over-voltages in the cable segment and lead to permanent cable insulation faults [45].

Lightning strike tests are important to conduct when developing new overhead transmission lines. Using a common standard lightning impulse to test power system equipment is necessary to secure reliability for all power systems.

It is also important to have specific standards for HVAC and HVDC systems. This secures the quality of the test that is performed and that all companies follow the same test procedures and can compare their results to other systems. There are two types of existing standard lightning impulses, the IEEE standard and CIGRE standard [46], [47]. The well-known IEEE standard lightning impulse is a 1.2/50 impulse, meaning an impulse with a wave front-time of 1.2 µs and a time-to-half-value of 50 µs [46].

2.4.3 DC circuit breakers and fault clearance

This section is taken from the specialization project with some improvements [6]:

For MMC transmission systems, DC fault isolation is said to be the most important challenge [48]. When a DC fault occurs, the faulted line needs to be isolated to prevent damage to other lines. VSCs are specifically vulnerable to this type of fault. The DC fault current needs, in general, to be interrupted in less than 20 ms to not get fault current levels above the withstand limit of the power equipment [49]. In this case, using an HVDC circuit breaker (CB) is the best approach to interrupt the DC fault currents to make it satisfies the requirements of both the DC grid and connected AC grids [49]. There exist several types of DC CBs, however, these have some disadvantages that can destroy other power equipment such as converters. Fault current interruption time and maximum current breaking capability are important criteria when choosing the most suitable CBs. The maximum current DC breaker capability needs to be higher than the current breaking capability for AC systems, due to smaller impedances on DC transmission lines.

MMC with half-bridge submodules does not have DC fault clearing capabilities [19]. To be able to clear the fault, CBs are needed on the AC side to disconnect the converter from currents from the AC side. This prevents diode damage, as diodes have low surge current withstand capabilities [16], [27]. A strategy to clear DC faults is to connect two thyristors in parallel to the submodules, to protect the diode and restart the system [50]. As LCC systems are based on thyristors, the converters can resist higher DC fault currents than VSCs. A few types of MMCs are able to achieve fault clearance without the need for CBs. Such types are MMCs with full-bridge submodules and MMCs with double-clamp submodules [50]. However, according to Raju et. al. (2018) [19], neither of these converters is in commercial use and the losses are also too high compared to half-bridge MMCs.

Traveling wave detection and fault location

The introduction to this chapter is taken from the specialization project with some improvements [6]:

Protection of power systems is in general a necessity to maintain the supply of power. Faults on the transmission line can be caused by, but are not limited to, environments like wind, lightning strikes, and ice. Other factors may be manufacturing processes, aging mechanisms, and human involvement (system design, system installation, and system operation). A good protection system is reducing the operating costs of a system by ensuring the operational status and reducing the system downtime. As the number of HVDC transmission systems grows, the need for good protection systems is greatly increased. VSC-based HVDC lines are difficult to protect, and high-speed protection is important in clearing faults due to high fault current [40]. VSC systems are specifically vulnerable to DC faults. This confirms the need for good protection systems.

Requirements for a good protection system can be seen below [51]:

- Selectivity: When a fault occurs, the system should isolate the fault by tripping only the necessary CBs to achieve this.

- Stability: The system should be able to stay unaffected by fault conditions occurring outside the zones of protection. A line with a fault should not affect the other lines surrounding it.

- Reliability: The system should be able to operate under all conditions. This includes having main protection and back-up protection for the system.

- Sensitivity: The system should be able to detect small faults as well as large.

- Speed: Faults should be cleared fast. This is to reduce damages as much as possible and quickly get the system into normal operation.

3.1   Traveling waves

The following paragraph is taken from the specialization project with some improvements [6]:

When a fault occurs on a transmission line, the fault will generate a TW due to rapid changes in voltage and current. The generated TW is an electromagnetic pulse consisting of high-frequency components up to 10MHz [52]. Waves are propagating in both directions from the fault position and toward terminals on each line end. The wave magnitude is at its highest close to the fault and will be decreased as the wave propagates along the transmission line due to line losses. Detecting TWs from the measuring device is the first indication that a fault has happened. The waves are moving near the speed of light and will reach the terminals within microseconds to milliseconds, dependent on the line length and fault position [52]. From a study conducted by GE in Brazil, it has been reported that TWs have enough energy to be detected even after 2300 km of propagation [5].

To understand how the wave velocity is dependent on the system parameters a circuit diagram of a cable can be used. Figure 3.1 shows an infinite cable with segment lengths denoted with Δx [43, p. 2.33]. y is the shunt admittance and z the series impedance.
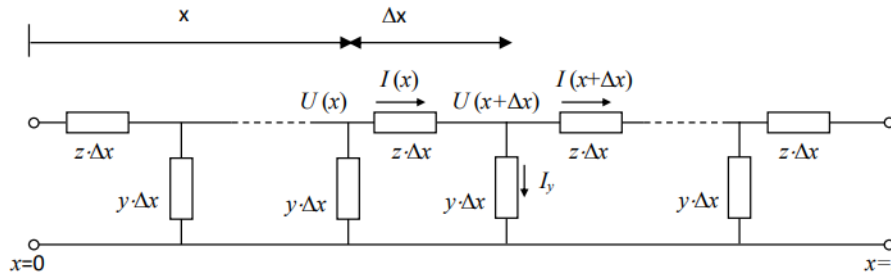
Figure 3.1: General circuit of an endless cable [43]

To analyze the behavior of generated waves, the wave equation can be derived. The wave equation is based on the circuit above and is given in (3.1). The general solution is given in (3.2). [43]

$$\frac{\delta^2 U(x,\omega)}{\delta x^2} = zyU(x,\omega) \tag{3.1}$$

$$U(x,\omega) = A(\omega) \cdot e^{-\gamma \cdot x} + B(\omega) \cdot e^{\gamma \cdot x} \tag{3.2}$$

The wave equation is a well-known equation describing the movement of waves, which is necessary when analyzing TWs. The solution of the equation contains the wave propagation constant γ. This constant consists of a real and imaginary part, shown in (3.3) [52]. The real part contains information about the propagation losses, showing that line losses occur as the wave propagates along the transmission line. The imaginary part describes the frequency dependency of the wave velocity [52].

$$\gamma = \alpha + j\beta \tag{3.3}$$

The wave velocity is dependent on several parameters, such as the fault position. As TWs contain different frequency components, the highest frequency components will reach a specific terminal before the lower frequency components [53]. This gives the waveshape of the wave with a steep change in the beginning, and a further decrease in the steepness before the wave reaches its top.

The velocity is dependent on other factors as well, such as the type of fault occurring and the resistivity of the soil [54]. It is also dependent on the use of overhead lines and cables. Due to the permittivity of the cable, the waves move with a lower velocity in cables compared to overhead lines [55].

The wave impedance is given in (3.4) [43, p. 2.34].

$$Z = \sqrt{\frac{z}{y}} = \sqrt{\frac{R + j\omega L}{G + j\omega C}} \tag{3.4}$$

In an ideal transmission line, R and G can be assumed negligible such that $Z = \sqrt{\frac{L}{C}}$ [56].

When a fault occurs and the TW is propagating along the line, a discontinuity on the line will make a part of the wave reflected and transmitted. This is illustrated in Figure 3.2 where the terminal is a discontinuity.
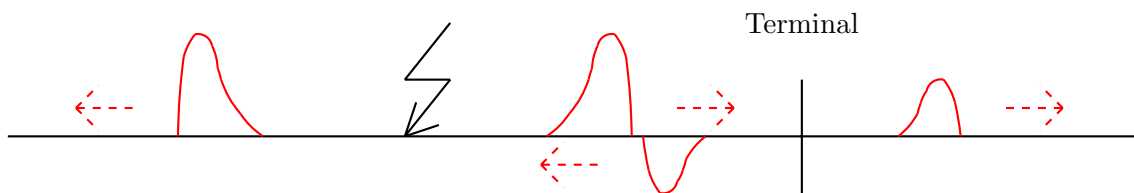
Figure 3.2: Illustration of reflection and transmission of TW at a terminal

How much of the wave that is reflected back or transmitted, is dependent on the impedances of the line [52]. The voltage and current reflection coefficients can be defined using (3.5) and (3.6) [44].

$$\rho_V = \frac{Z_T - Z_C}{Z_T + Z_C} \tag{3.5}$$

$$\rho_I = \frac{Z_C - Z_T}{Z_T + Z_C} \tag{3.6}$$

Z_T is the impedance at the terminal and Z_C is the line impedance. The reflection coefficients describe how much of the incoming wave is reflected back. Thus, if one of the reflection coefficients is 1, corresponding to Z_T being zero or infinite, there will be a complete reflection of the wave [44]. For reflection coefficients of zero, the wave will be transmitted and no reflection will occur.

3.2   Tools for measurements and signal processing

3.2.1   Measurement systems

The measurement system structure depends on how many measuring devices are needed for a specific fault detection system. By using more than one measuring device for a specific transmission line segment, the devices need a communication strategy to work properly. This is achieved with the use of GPS to obtain a common time standard [57]. GPS receivers receive data pulses from satellites with satellite positions and reference times corresponding to the time each satellite sent out the signal [58]. It is stated that a precision time synchronization with an accuracy of 100 ns is preferred [52], [58]. Figure 3.3 gives an overview of the measuring system with two relays. The relays send data to a central processing unit for the data to be analyzed [4].
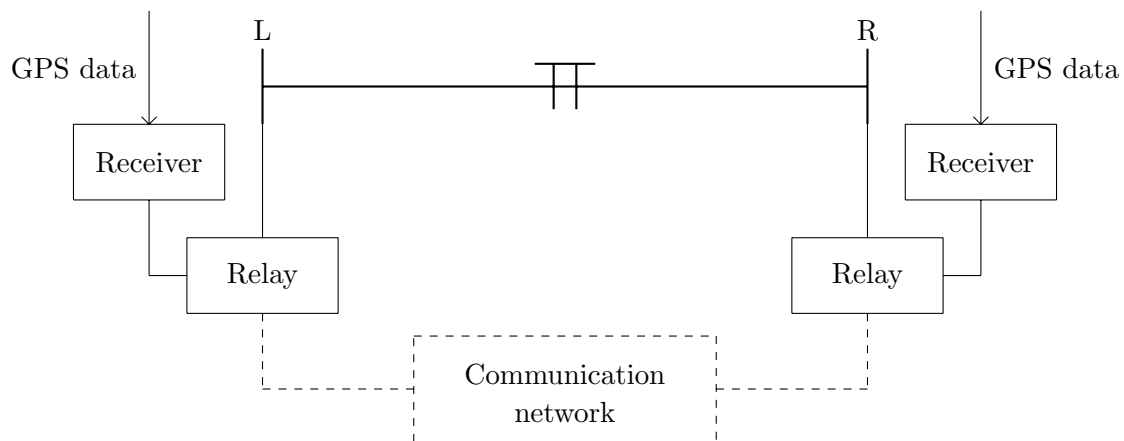
Figure 3.3: Overview of the communication setup principle when using two measuring relays

Time synchronization between devices is important to ensure that the waves measured are located accurately in time. Another parameter that is important for detecting waves is the sampling rate or sampling time. Sampling is the process where measuring devices take so-called snapshots of the system parameters at specific time intervals [59]. The sampling rate is given in Hz and is the inverse of the sampling time. A lower sampling rate makes the results more accurate as the signals are measured with shorter time intervals.

Accurate measuring devices are needed to catch voltage and current transients at a certain sampling frequency. For HVDC transmission line measurements, conventional VTs and CTs are not appropriate to use [5]. resistive voltage dividers and optical voltage dividers are suggested as better choices for DC measurements [5]. However, resistive voltage dividers are said to have poor frequency performance [60]. Instead of these, resistive-capacitive voltage dividers are a popular choice for voltage measurements [59], [61].

The structure of the resistive-capacitive voltage divider is given in Figure 3.4 [37].
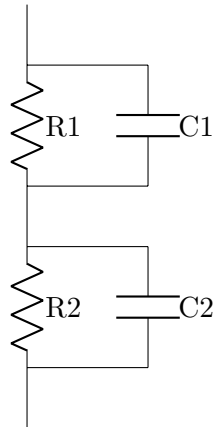
Figure 3.4: Resistive-capacitive voltage divider

For current measurements, the Rogowski coil is stated to be a good option to detect transients [4], [62]. The principle of the Rogowski coil is that it generates a voltage based on the mutual inductance and the derivative of the current. The generated voltage is given in (3.7) [62].

$$e_0(t) = M\frac{di(t)}{dt} \tag{3.7}$$

It has been seen that the Rogowski coil detects TWs in an accurate way because it measures zero current for steady-state DC currents [4].

In addition to proper measuring devices, the choice of sampling rate is important for accurate TW detection. The reason for this is illustrated in Figure 3.5 [59, p. 93]. The x-axis is given in time in µs. A sampling time of 1 µs corresponds to a sampling rate of 1 MHz. A higher sampling rate will give a more accurate wave detection as seen in the figure. It can also be seen that a sampling time of 10 µs, equal to 100 kHz sampling rate, gives a poor wave detection capability. A sampling rate of 1 MHz is said to be a minimum requirement to achieve accurate measurements [59, p. 92]. In the fault HVDC location study in Brazil a sampling rate of 5 MHz was used [5].
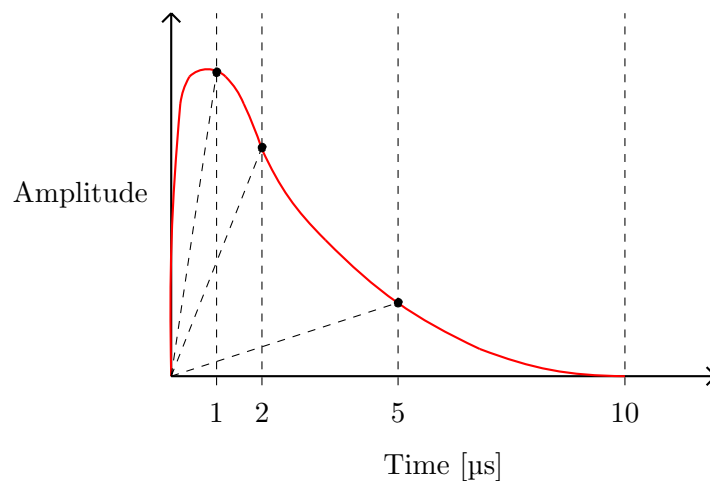
Figure 3.5: Illustration of how the sampling time can influence TW detection

3.2.2   Signal processing

Several analysis tools have been developed during the past years for signal processing. The well-known Fourier transform is converting a signal from the time domain to the frequency domain. However, this is not optimal for time-varying transients as the frequency obtained will not be time-dependent [63], [64]. This is where the wavelet transform comes into its right place, as a further development of the Fourier transform [65]. Compared to the Fourier transform, the Wavelet transform can also provide the time of the frequency components of the signal [66]. This is shown to the right in Figure 3.6 [64]. Thus, wavelet transformation is used for signal and data processing and is a well-suited mathematical tool for TW fault detection and location.
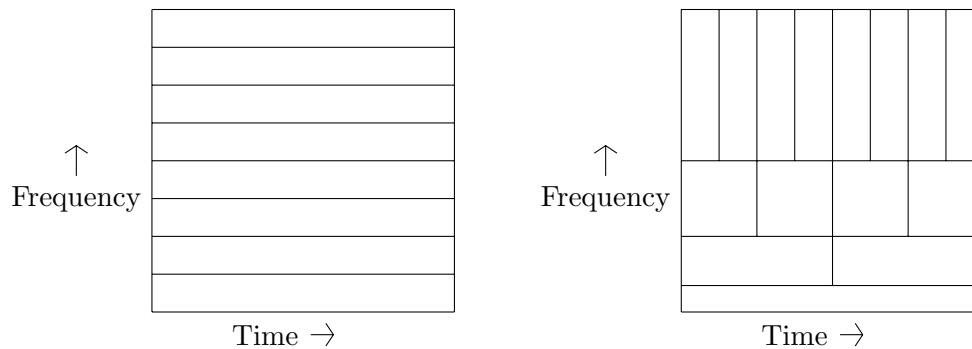
Figure 3.6: General Fourier transformation (left) and Wavelet transformation (right)

3.2.3   Wavelet transformation

A signal can be either continuous or discrete. A continuous signal can be described as a function where the information can always be obtained to a specific accuracy. Discrete signals are sampled at a certain sampling rate. For TWFL studies, discretely sampled data is collected by measuring devices and analyzed by the processing unit. Two types of wavelet transformation can be used to process these sampled data, the continuous wavelet transform (CWT) and the discrete wavelet transform (DWT) [67].

CWT

The continuous transformation provides a detailed and continuous analysis of a signal [68]. The formula for obtaining the CWT coefficients from a signal $x(t)$ is given in (3.8) [65].

$$W(a,b) = \frac{1}{\sqrt{|a|}} \int_{-\infty}^{+\infty} x(t)\psi^* \left(\frac{t-b}{a} \right) dt \qquad (3.8)$$

a is the scaling factor and b is the shifting factor. These factors are continuously varying. The input signal is multiplied with the convolution of the mother wavelet $\psi()$ as the wavelet moves through the signal. The mother wavelet functions as a band-pass filter, passing through frequencies at a certain range and removing frequencies outside this range [68], [69].

The type of mother wavelet can be varied depending on what is most suitable for the specific signal $x(t)$ [70], [71]. All wavelet functions have average values of zero, this is shown in (3.9) [68], [69].

$$\int_{-\infty}^{\infty} \psi(t)dt = 0 \tag{3.9}$$

The scaling factor is either compressing or stretching the wavelet. A high scale stretches the wavelet, thus making it capture low-frequency components. A low scale is however compressing the wavelet, enabling it to capture higher frequency components [69]. The Morlet wavelet is one of the frequently used wavelets when applying CWT [68]. An example of scaling of this wavelet is given in Figure 3.7.

| (a) Compressed | (b) Original | (c) Stretched |
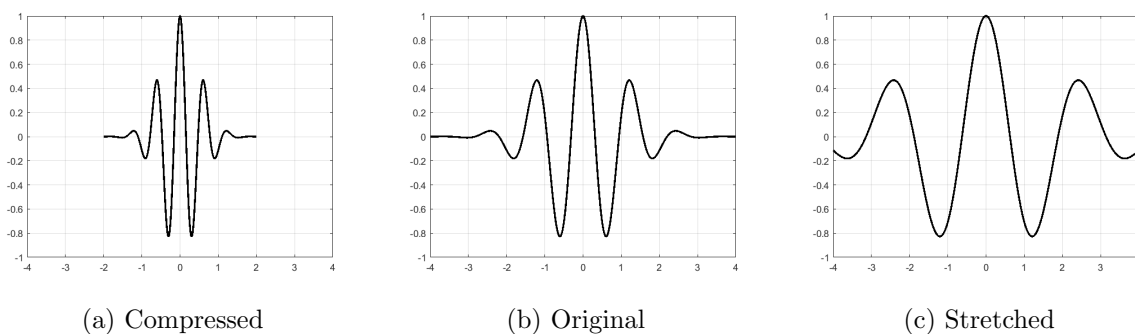
Figure 3.7: Scaling of the Morlet wavelet

The wavelet in the middle shows the Morlet wavelet with $a = 1$. The wavelet to the left is compressed with $a = 0.5$, while the wavelet to the right is stretched with $a = 2$.

The shifting factor b is moving the wavelet smoothly along the time axis of the input signal. CWT is able to use any specified scale up to a maximum accuracy dependent on the original signal [68]. As a result of these variations in scaling and shifting, the CWT coefficients are obtained for each set of a and b.

DWT

The DWT is a simplification of CWT, sampled on a dyadic grid [66]. This makes DWT a less accurate method compared to CWT. The equation for the DWT coefficient can be obtained by replacing a with a_0^m and b with ka_0^m, where $a_i = 2^i$ [66]. This equation for the continuous transformation in (3.8) can now be written using the discrete form as in (3.10).

$$W(m,n) = \frac{1}{\sqrt{|a_0^m|}} \sum_k x(k)\psi^*(\frac{n - ka_0^m}{a_0^m}) \tag{3.10}$$

DWT is conducted by applying a filter bank with a specific amount of levels to the signal, this can be seen in Figure 3.8 [66], [72].

When the input signal is detected, it is sent through a high-pass filter and a low-pass filter. A low-pass filter is a filter passing the frequency components below a set cutoff frequency, while high-pass filters pass components above the set cutoff. Based on the use of low- and high-pass filters at different levels, coefficients are obtained.
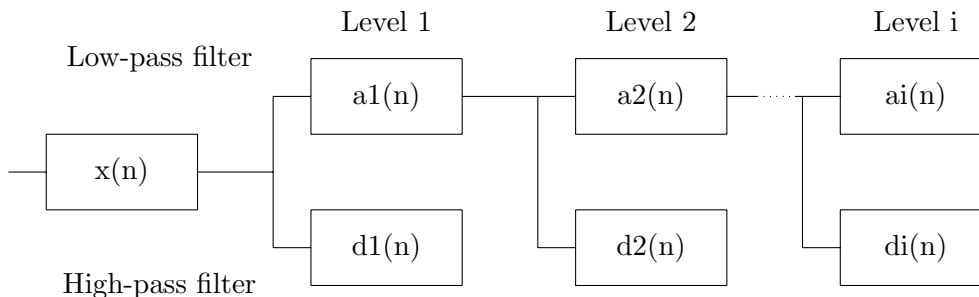
Figure 3.8: Illustration of DWT filter bank

The original signal x(n) has a frequency of f and will contain components from 0 Hz to f Hz. The signal is sent through high-pass filters and low-pass filters at the same time. The first high-pass filter results in the wavelet detail coefficient, d1(n), at level 1. This is shown in the figure. d1(n) contains the frequency components from f/2 Hz to f Hz [72]. The approximation coefficient a1(n) however, contains the frequency components from 0 Hz to f/2 Hz, as a result of x(n) passing through the low-pass filter. The approximation coefficient is therefore an approximated version of the original signal, but now with a bandwidth from 0 Hz to f/2 Hz. This signal is again sent into a new low-pass and high-pass filter, resulting in level 2 detail and approximation coefficients. The bandwidth at the next levels is further reduced until a certain specified level i is achieved. The approximation coefficients give the approximated and simplified versions of the original signal x(n). The detail coefficients, however, show discontinuities of the signal [73].

DWT is an easier tool to use because of its simplicity and because it is less demanding to compute compared to CWT [70]. Thus, DWT has often been a preferred option as it is more simple and still gives good results. A common wavelet used for TW fault detection on the discrete form is the Haar wavelet ($db1$) [63], [70]. This wavelet is a step function and is the simplest wavelet, therefore it is easy to use. It is also said to be one of the best wavelets to detect the first incoming wave [63]. Other mother wavelets can also be used for DWT. A study conducted on the influence of mother wavelet choices for DWT in an HVAC system showed that the Daubechies wavelet ($db4$) had better accuracy than both the Coiflets wavelet ($coif4$) and Symlets wavelet ($sym4$) [73]. da Silva et. al. (2019) [63] also states that $db4$ is one of the best options. Several papers state, however, that CWT gives more accurate results of fault location compared to DWT [68], [70].

3.3   Traveling wave protection

TW protection is often used as the main protection of HVDC transmission lines [56]. Incoming TWs are the first sign of a fault and this protection method is there much faster than impedance-based methods. This is important for DC faults. Minimum and maximum voltage operation limits are always set for a transmission line, and there are also limits for the fault current. Usually, voltage limits are set to a minimum of 0.9 pu and a maximum of 1.1 pu [74]. For fault currents, the limits are dependent on the component with the worst current tolerance. Devices are continuously sampling line voltages and currents and comparing these to the threshold.

A register such as COMTRADE is normal to use to capture incoming waves as it is described in [5]. When a set threshold is exceeded it triggers the recording of the signal. In [5], they used a method where the recorded signals were timed 100 ms before the trigger started and 16 ms after the trigger started.

This protection method is stated to be challenging for very long transmission lines and high impedance faults, as the waves will be more damped [56]. Another challenge for TW protection is if a very short transmission line is placed on the other side of the measuring terminal [44]. The reflected incoming waves can then be disturbed by waves reflected from the opposite end of the short transmission line. Therefore it is important that the protection system is able to distinguish between forward and backward TW. This can be utilized by looking at the TW current polarities [59, p. 60].

3.4   Fault location methods

TWFL can be achieved in different ways. The most common approaches are using double-ended or single-ended methods. The double-ended method is using measurements on two different terminals, while the single-ended is using measurements at one terminal to locate faults. These two methods will be further explained in this section.

3.4.1   Double-ended TWFL

The double-ended TWFL method is based on measuring the fault response on two terminals. The terminals are located on each side of the protected transmission line. This method has the advantage of being easy to implement, however, it requires two relays, each using a common time reference to obtain time synchronization of the incoming measurement signals [52]. This has already been described in Section 3.2.1. In Figure 3.9, a fault occurring on a transmission line is illustrated, and the generation of TWs, and their reflections and transmission, are shown [44].
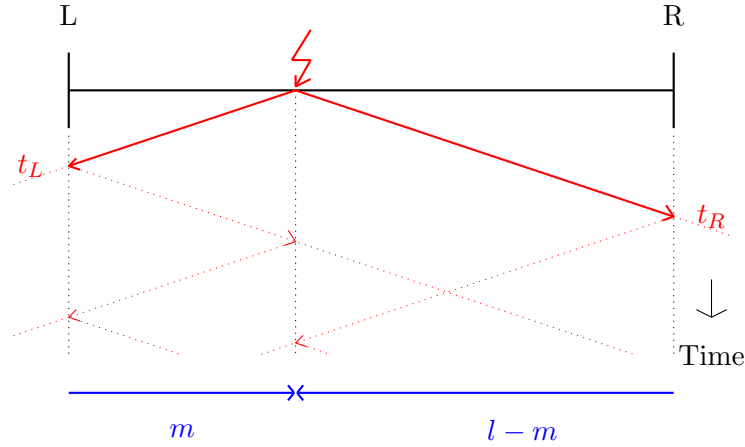
Figure 3.9: Double-ended TWFL principle for a transmission line with terminals L and R

t_L and t_R correspond to the time arrivals for the first TW on each of the terminals. The dotted lines show the reflections and transmissions of these two waves. m is the distance from terminal L to the fault, and $l - m$ is the fault distance from terminal R.

Based on this figure, equations for the fault distances can be obtained. These time arrivals are used to calculate the fault locations, given in (3.11) and (3.12) [75].

$$m = \frac{l - v(t_R - t_L)}{2} \tag{3.11}$$

$$l - m = \frac{l + v(t_R - t_L)}{2} \tag{3.12}$$

v is the wave velocity and l is the total line length.

3.4.2 Single-ended TWFL

Compared to the double-ended TWFL method, the single-ended method only needs one measuring device. Thus, the overall cost of implementation is reduced. This method is dependent on the reflection and transmission of TWs [72]. Figure 3.10 shows the principle of this method, using terminal L as the measuring terminal. Faults on the first and second half of the transmission line are shown, and it can be noticed how the incoming waves depend on the fault position. To the left is a fault occurring on the first line half. In this case, the second incoming wave at the measuring terminal is reflected from the fault. The third incoming wave shows that the reflected wave from the fault and the reflected wave from the opposite terminal arrive approximately at the same time at the terminal. To the right in Figure 3.10, the fault is closer to terminal R. t_2 is now the arriving time of the reflected wave from the opposite terminal, while the third incoming wave is the reflected wave from the fault. The time arrivals of the two first incoming waves, t_1 and t_2, are usually used to calculate the fault location [66], [72].
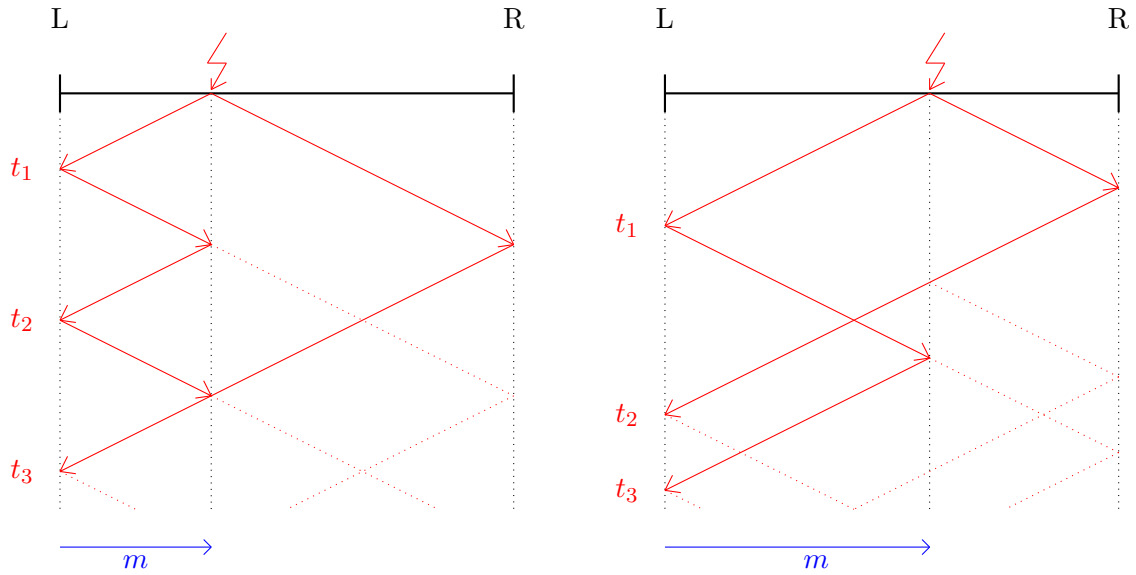
Figure 3.10: Comparison of TW arrival times for a fault on the first half and on the second half of the transmission line

One of the big challenges regarding the single-ended TWFL method is determining on which half of the line the fault is occurring [66], [72], [76]. This is necessary because there are different formulas dependent on which half the fault occurs. The algorithm needs to determine if the second incoming wave is reflected from the fault or reflected from the opposite terminal.

In [72], the authors state that by looking at the magnitudes of the first and second incoming waves, in addition to the ratio between the first and second wave peaks, one would be able to determine where the second wave comes from.

Fault location considering the first two incoming waves

A common method is two consider time arrivals for the first two waves. By determining where the second wave is reflected from, the following formulas, (3.13) and (3.14), are used for fault location [72]:

For a fault occurring on the first half of the transmission line:

$$m = \frac{t_2 - t_1}{2}v \tag{3.13}$$

For a fault on the second half of the transmission line:

$$m = l - \frac{t_2 - t_1}{2}v \tag{3.14}$$

l is the total line length and v is the wave velocity.

Fault location considering the three first incoming waves

Altay et. al. (2014) [76] suggest another fault location algorithm to locate faults. This method will now be introduced. It is based on information from the three first incoming waves and their time differences. By using this, there is no need to include the wave propagation speed in the fault location equations. However, it is still important to know if a fault is very close to the terminal or further away, as one needs to use different formulas for calculating the fault position.

To check if a fault is close to a terminal the authors use the condition given in (3.15).

$$t_2 - t_1 = t_3 - t_2 \tag{3.15}$$

If this is fulfilled, the fault is close to one of the terminals. Thus the following equations, (3.16) and (3.17), can be used to locate the fault dependent on which half the fault is occurring. t_{ref} is the first incoming wave reflected from the opposite terminal.

For a fault on the first half of the transmission line:

$$a = \frac{(t_2 - t_1)l}{t_2 - 2t_1 + t_{ref}} \tag{3.16}$$

For a fault on the last half of the transmission line:

$$a = \frac{(t_{ref} - t_1)l}{t_2 - 2t_1 + t_{ref}} \tag{3.17}$$

If a fault is further away, the second and third incoming waves are not reflections from the same place, and (3.15) will not be fulfilled. Thus the following formulas (3.18) and (3.19) can be used to locate the fault.

For a fault on the first half of the transmission line:

$$a = \frac{(t_2 - t_1)l}{t_2 - 2t_1 + t_3} \tag{3.18}$$

For a fault on the last half of the transmission line:

$$a = \frac{(t_3 - t_1)l}{t_2 - 2t_1 + t_3} \tag{3.19}$$

3.4.3   Obtaining information from wavelet coefficients

With the basic principles of wavelet transformation and the TWFL methods explained, it is important to understand how wavelet coefficients are used to detect TWs from a fault. This example is for a pole-to-ground fault in an HVDC system, where a fault is occurring after 5.05 s. The model is obtained from an MMC example model and is a bipole MMC half-bridge model [77]. The faulty pole voltage is measured at the terminal near the MMC rectifier and is given in Figure 3.11.
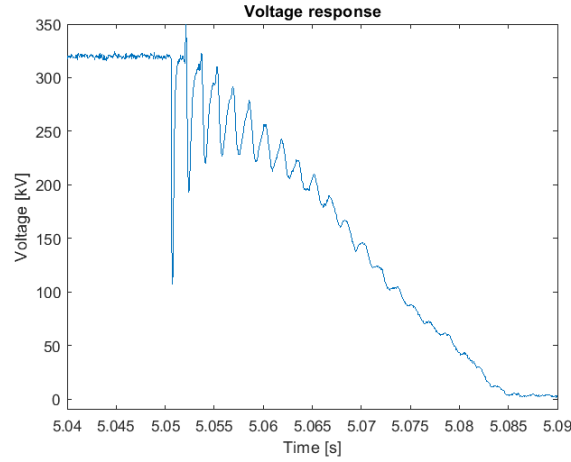
Figure 3.11: Voltage response of faulty pole measured close to the MMC rectifier

This voltage response works as an input signal when applying wavelet transformation. This example will use DWT and the Haar mother wavelet to show how the wavelet coefficients are obtained. By applying two levels of DWT, approximation coefficients and detail coefficients can be obtained. Figure 3.12 shows the approximation coefficients at both levels. The approximation coefficient on level 2 (a2) contains only the bottom half of the frequency components of the level 1 approximation coefficient (a1). Thus, a1 contains the frequency components from $0\,\text{Hz}$ to f/2 Hz while a2 contains the components from $0\,\text{Hz}$ to f/4 Hz. This means that an approximation coefficient on higher levels gives a more smooth response as the highest frequency components are not considered.

(a) a1

(b) a2
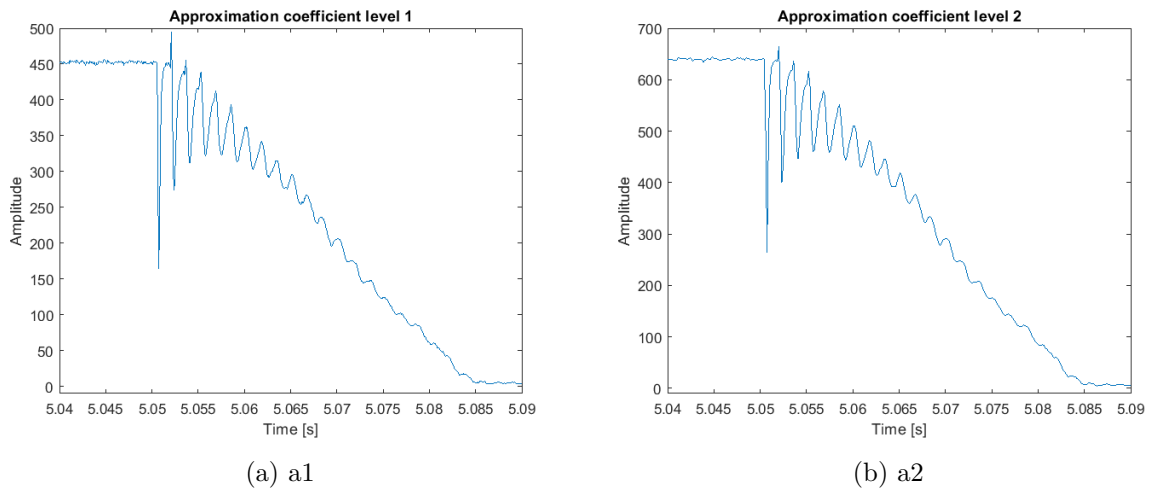
Figure 3.12: Approximation coefficient based on voltage response example for Haar level 1 and level 2

The x-axis is, in this case, showing the time. This is to make the graphs easier to read. The wavelet coefficients originally give the sampling numbers on the x-axis.

The detail coefficients are also obtained for level 1 (d1) and level 2 (d2). d1 contains the highest frequency components from f/2 Hz to f Hz and has a higher sampling rate compared to d2 which contains the components from f/4 Hz to f/2 Hz. By analyzing these coefficients, the waves can be detected and located in time. In Figure 3.13, the two first waves are circled for both d1 and d2. The time location of the first wave is marked t1 and the second wave is occurring at t2. As explained in the single-ended method, the time parameters t1 and t2 are used in the equation for the location of the fault.

(a) d1   (b) d2
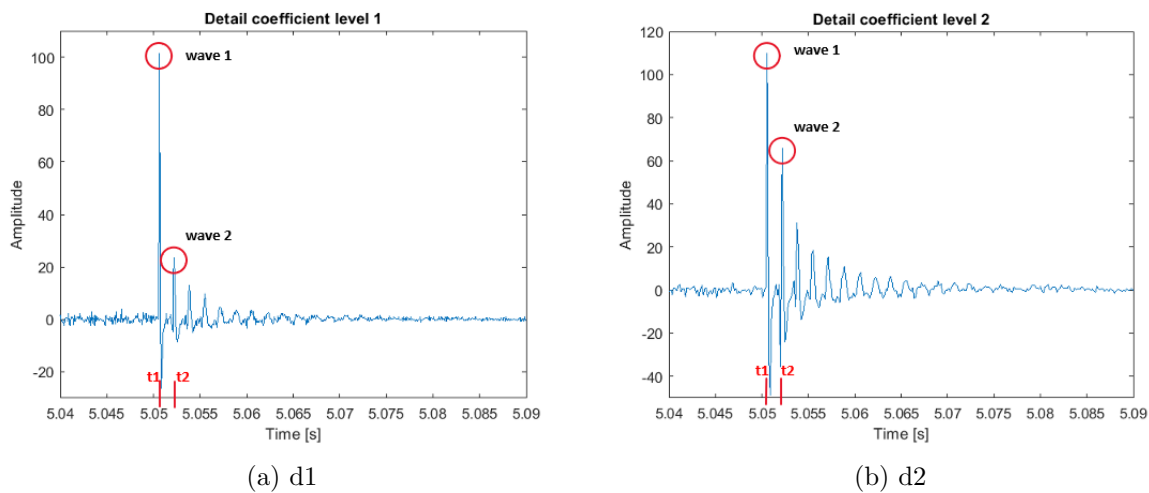
Figure 3.13: Detail coefficient based on voltage response example for Haar level 1 and level 2

3.4.4   Other novel TWFL methods

In this section, some examples of novel methods for fault location are given. The general fault location principles introduced have been based on one transmission line segment. Regarding fault location on hybrid transmission lines consisting of overhead lines and cables, some studies have been conducted where the measuring terminals were placed on each converter end [4], [78].

Using a correct wave velocity has been described to be challenging, as this depends on several factors. In addition to this, has time synchronization been mentioned as a challenge for fault location accuracy when using double-ended methods. Ding et. al. (2017) have proposed a solution to these challenges [79]. By using three measuring points instead of two, one of the points is located in the middle of the transmission line. The middle point is used to connect the other terminals. With this method, it is easier to obtain the correct wave velocity and the time synchronization problem is also not an issue.

When it comes to signal processing, there have been some different approaches. One example is using a signal fitting method based on the generalized logistic function before applying wavelet transformation [53]. With this method, the zero-mode and line-mode fault currents are used to calculate the fault location. In [80], a fault location method where the DC line voltage, line current, and the reverse voltage are used as input signals for DWT is proposed. A third example is using the real-time stationary wavelet transform (RT-SWT) instead of the conventional wavelet transforms [63].

3.5   TWFL products on the market for HVDC

The features of HVDC systems require measurement devices suitable for DC, and thus fault location products that can handle DC faults. Since TW protection has become more and more popular for both HVAC and HVDC lines, information about TWFL products for HVDC lines has become available. However, there are only two specific fault locators that seem to be publicly available. These are given below:

- **GE** is an electric company founded in 1889 [81]. This company is well known for technologies used for transmission systems. RPV311 is a fault recorder system applicable for AC and DC systems [82]. RA333 is also an important part of the TWFL system. GE has been focusing on fault location for HVDC lines for several years, by publishing a study on traveling wave fault location on HVDC lines in Brazil in 2018, where the accuracy was on average less than $0.01\,\%$ of the line length [5].

- **Kehui** was founded in 1991 and is a company for technology development located in England and China [83]. They have a traveling wave fault locator system called XC-2100E, which is suitable for faults on HVDC lines with an accuracy of ± 150m [84].

Other large companies such as Hitachi, Siemens, and SEL (Schweitzer Engineering Laboratories) are offering fault locators based on the use of TW, however, it is difficult to find information about fault locators specified for HVDC systems.

Chapter 4

Simulation and fault location methodology

This chapter presents the implementation of the HVDC-MMC model in PSCAD and the TWFL algorithm in MATLAB. It starts by explaining the PSCAD model and gives an overview of the power system incidents that have been simulated for fault location testing. Further, the fault location algorithms are explained, and different decisions that have been made during implementation are justified. Parameters and information regarding this chapter are given in Appendix A, Appendix B and Appendix C.

4.1   PSCAD modeling

The HVDC-MMC model is as described earlier based on the Nordlink interconnector and modeled in PSCAD. The following introductory part is taken from the specialization project [6]:

Power Systems Computer Aided Design (PSCAD) is a graphical user interface using the Electromagnetic Transients including DC (EMTDC) software. This is a suitable choice for transient simulations with power electronics in HVDC systems. Some basic assumptions are necessary when modeling using PSCAD/EMTDC [85]:

- The earth is flat along the whole transmission line

- The earth is homogeneous with constant resistivity

- Conductors are modeled as perfectly round cylinders

Temperature changes have not been considered for the simulations. The DC resistances for the overhead line and cable conductors were given for a temperature of 20 °C. The "Frequency Dependent (Phase) Model" was used to obtain an accurate transient behavior of the system. DC correction was disabled for all transmission lines. Necessary transmission line parameters were obtained from Statnett, the Transmission System Operator (TSO) of the Norwegian power system.

4.1.1 Implementation of the HVDC-MMC system

The first step to model the HVDC-MMC system was to implement the MMCs. It was necessary to include both the MMC rectifier and inverter in order to be able to control the system parameters properly. Implementing an MMC system is complicated, therefore a general HVDC-MMC model available on the PSCAD homepage from a seminar in 2015 was used [77]. A simple sketch of the most central parts of the system is presented as a one-line diagram given in Figure 4.1. This figure shows a system with a DC grid consisting of an overhead line and a sub-sea cable. The underground cable on the German side is not relevant in this model. MMCs are used for conversion between AC and DC, and AC grids are placed on both sides. On the Norwegian AC side, the voltage level is 420 kV, while it is 380 kV on the other German side [1]. The DC voltage level is 515 kV. In PSCAD, the system was implemented with a bipolar configuration.
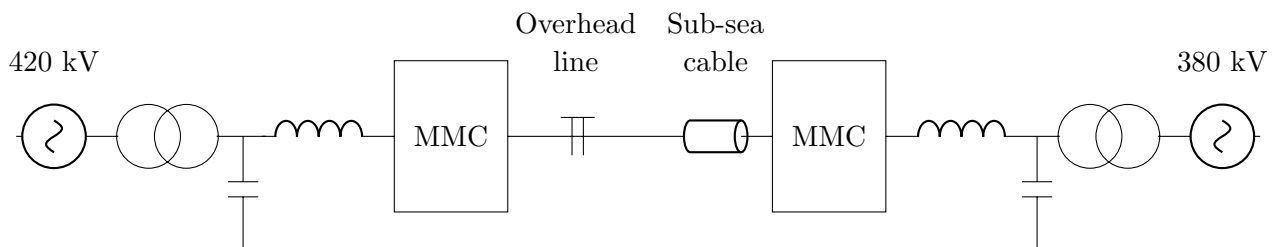
Figure 4.1: One-line diagram of the HVDC-MMC system model

Since the bipolar HVDC-MMC model was obtained from the PSCAD homepage, most of the settings were kept unchanged. To obtain the correct voltage levels with voltage ripples within acceptable limits, some settings were adjusted. For active power transmission, the settings were set for active power export of in total 1400 MW. This corresponds to 700 MW for each pole. The system parameters that have been changed compared to the original model are presented in Table A.1.

4.1.2 Overhead line and sub-sea cable

The models of the overhead line and sub-sea cable were based on models developed in the specialization project [6]. As the NordLink interconnector has a bipolar configuration, two parallel coaxial cables were needed. This is shown in Figure 4.2b. The cables are equal in geometry and layers, only with different voltage polarities. Cable 1 is the positive pole of the system while Cable 2 is the negative pole. Parameters for these cables were obtained both from Statnett and from Bremnes and Evenset (2015) [86]. Table A.2 provides the necessary parameters used in the cable model.

(a) Overhead line   (b) Sub-sea cables
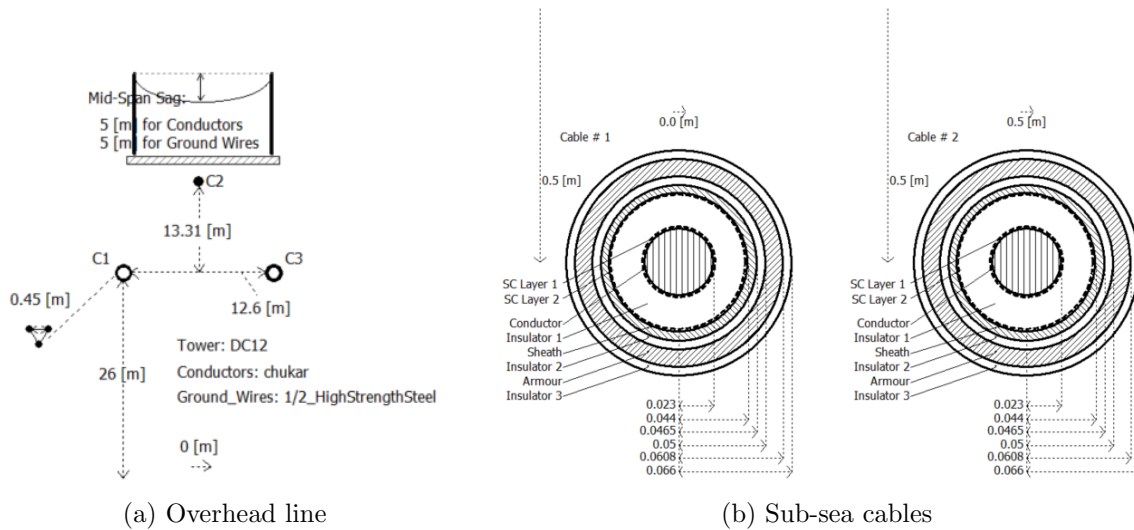
Figure 4.2: Geometries for transmission line segments in PSCAD.

The overhead line was modeled using the DC2 model from PSCAD shown in Figure 4.2a. For the real NordLink overhead line, two types of tower configurations exist. However, the PSCAD model was simplified by using only one type. The DC2 tower model represents a flat two-conductor model giving the option of one or two ground wires placed on a higher level than the two conductors. The two poles are named C1 (positive pole) and C3 (negative pole), modeled as a bundle configuration with 3 sub-conductors. By disabling ground wire elimination, the ground wire was treated as a standard conductor. The ground wire was named C2 and is seen in the tower configuration above. A consequence of including the ground wire was that DC correction had to be disabled for all transmission line segments.

By comparing this overhead line with the overhead line from the original PSCAD MMC example model, the example model used ground wire elimination. Thus, it only used two conductors. Therefore, the ground wire had to be added to the system model manually in order to achieve 3 conductors in the overhead line. This is shown in Figure 4.3. A three-line-breakout component replaced the two-line-breakout component. The ground wire is the middle line and has no signal source. As the ground is not ideal, a resistance of $1\,\Omega$ was added on each end of the ground wire [38]. The tower grounding resistance was chosen to be $20\,\Omega$ [43, p. 103]. This is a simplification of real physical overhead line towers, where this resistance varies.
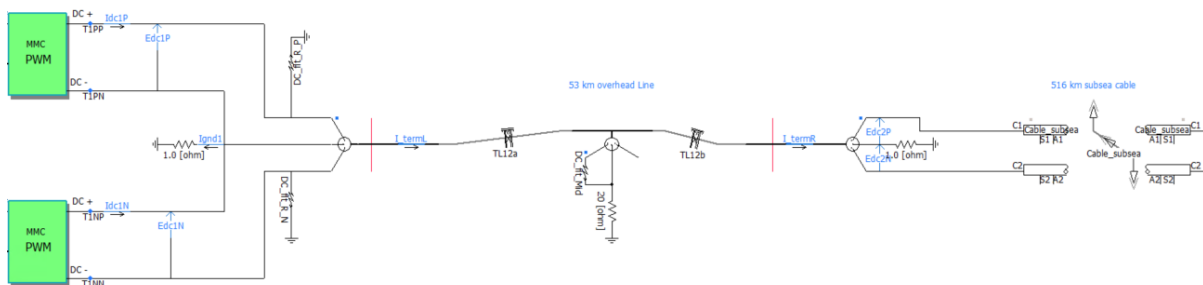
Figure 4.3: A part of the PSCAD model showing the implementation of the ground wire on the overhead line

4.1.3   Simulation studies

A sampling time of $2\,\mu s$ was used when simulating. This implies a sampling rate of $500\,kHz$. The main goal was to use a sampling rate of $1\,MHz$, which is described to be the minimum value for proper traveling wave detection in Section 3.2. However, this was not possible to achieve with this system, due to possible failures in the mathematical computations of the MMC. It made the output signals behave non-realistic and did not achieve steady-state operation.

Several different power system cases were simulated for TWFL testing. From Section 2.4, the most common type of faults on DC overhead lines was said to be pole-to-ground faults. This type of fault has therefore been simulated with variations in fault parameters. In addition to this, different power system incidents have been applied, lightning strikes and AC grid disconnection. Lastly, an HVDC transmission system based on DC voltage sources was developed. This model contains the same transmission line segments as the original model of the HVDC-MMC system, and these two models have been compared. The different cases are described in more detail below:

- **Variation in fault position**: It is important to test how the traveling wave algorithms are able to locate faults close to the terminals and further away. The different applied fault positions are given in Table 4.1. The positions correspond to a total overhead line length of $53\,km$. These cases were simulated for a pole-to-ground fault occurring on the positive pole at time $0.05\,s$ and fault resistance $0.1\,\Omega$.

Table 4.1: Overview of fault positions with reference to terminal L

Test number	1	2	3	4	5	6	7
Position [%]	5%	15%	35%	50%	65%	85%	95%
Position [km]	$2.65\,km$	$7.95\,km$	$18.55\,km$	$26.5\,km$	$34.45\,km$	$45.05\,km$	$50.35\,km$

- **Variation in fault resistance**: Fault resistances of $0.1\,\Omega$, $10\,\Omega$ and $100\,\Omega$ were simulated for the fault positions $18.55\,km$, $26.5\,km$ and $34.45\,km$. This is to observe if fault resistance variations influence the fault location accuracy. These cases were simulated for a pole-to-ground fault occurring at the positive pole at time $0.05\,s$.

- **Power system incidents**: Power system incidents such as lightning strikes at fault positions $18.55\,km$ and $34.45\,km$, and AC grid disconnection, have been simulated. Lightning strikes were applied on the overhead line ground wire and directly on the positive pole to simulate shielding failure.

  To implement a lightning strike, a surge generator was needed as an external signal source feeding a DC current source. The lightning current is almost independent of the object that is hit, this is why a current source is usually applied to simulate lightning strikes [43, p. 3.88]. The lightning strike generator is shown in Figure 4.4. For this generator, the IEEE standard function was chosen. This is mentioned in Section 2.4 to be the 1.2/50 standard impulse.
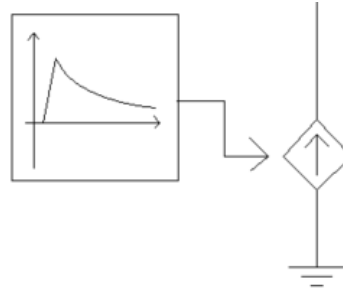
Figure 4.4: Lightning strike generator modeled in PSCAD

Table 4.2 shows the different lightning strike tests that was performed:

Table 4.2: Overview of lightning strike tests with the applied amplitudes

Fault position	Ground wire strikes	Shielding failure strikes
18.55 km	3 kA 50 kA 100 kA	3 kA 10 kA
34.45 km	3 kA 50 kA 100 kA	3 kA 10 kA

AC grid disconnection was further simulated by opening the CB in the 420 kV AC grid after 0.05 s. A power system incident like this is not DC a fault. However, transients will still occur due to rapid changes in system voltages and currents as the AC source is no longer able to feed the DC transmission line from the 420 kV side.

- **HVDC-MMC model vs. DC voltage source model**: The implementation of the HVDC-MMC system could only use a time sampling of 2 μs, however, it should be possible to use a smaller sampling time with a more simplified model containing less complicated system computations. To investigate if modeling the HVDC-MMC system is necessary for obtaining realistic fault responses and accurate fault location, a model based on DC voltage sources has been developed. This model does only show the DC grid with a voltage of 515 kV and is shown in Appendix B.

The faults on the DC voltage source model were applied for sampling times of 2 μs and 1 μs. This corresponds to 500 kHz and 1 MHz sampling rates. This was to test how a lower sampling time influences the fault location accuracy. These results were compared to the results of the original MMC model. Fault positions of 18.55 km and 34.45 km have been used to have faults on both the first and the second half.

4.2 Traveling wave fault locator in MATLAB

As mentioned in Section 3.2.2, wavelet transforms are utilized to obtain both time and frequency characteristics of a signal. In the Wavelet toolbox in MATLAB, there are different mother wavelets available. It is crucial to select the appropriate wavelet that is suitable for the specific problem and is computationally achievable. CWT was initially used as it is said to be the most accurate method. However, after testing this method it was too demanding for the MATLAB software to compute within a reasonable time. This made DWT a better option for implementation. As explained in Section 3.2.2, DWT has been proven to deliver good results while being the simplest and least computationally intensive method.

The Wavelet toolbox makes it possible to compute the wavelet transform both in the toolbox itself and by manually coding it in MATLAB. Manual MATLAB coding was the chosen option as the TWFL algorithm should analyze the incoming signals automatically. When using DWT, the wavelet type options were many [71]. However, as seen in Section 3.2.2, the Haar (*haar or db1*) wavelet and Daubechies (*db4*) wavelets are stated to be good choices. As the Haar wavelet is said very optimal at detecting the first wave, this wavelet was chosen as the mother wavelet in this study. As explained earlier, several levels of the wavelet coefficients can be used. The proposed algorithm should be able to locate the fault in the most accurate way. By choosing the Haar mother wavelet on level 1, the detail coefficients consist of the highest frequencies and the sampling rate is at its highest.

In this work, the TWFL algorithms were only used for fault location within the fault location zone. Only faults occurring on the transmission overhead line should be located. This is shown in Figure 4.5 as the red area between terminal L and R. The number of measuring devices is dependent on the choice of double-end or single-end TWFL algorithm. The measuring terminal R was placed between the overhead line and the cable because the wave would be expected to move slower through the cable. It would therefore give a better fault location accuracy to place the measuring devices on both sides of the overhead line segment.
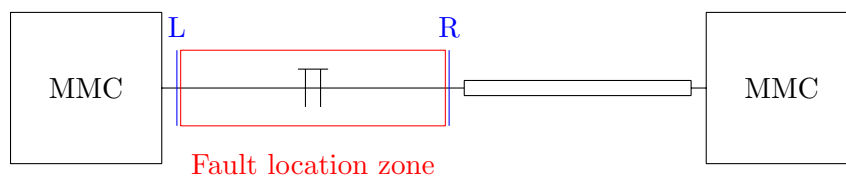
Figure 4.5: Illustration of the fault location zone and measuring terminals L and R

The fault locations obtained from the algorithm were compared to the real fault positions set in PSCAD, and the errors were estimated using (4.1)

$$error(\%) = \frac{loc_{L,R} - loc_{real}}{loc_{real}} \cdot 100\% \tag{4.1}$$

where $loc_{L,R}$ is the fault location obtained from the algorithms and loc_{real} is the fault position set in PSCAD.

4.2.1 Test case

When developing fault location algorithms based on DWT, input signals were needed. A test case was run to determine if the input signals should be based on voltage signals or current signals, or a combination of both. The test case was a positive pole-to-ground fault occurring in the middle of the overhead line, at fault position 26.5 km from both terminals. GPS synchronization was ideal as the input signals were obtained and loaded from PSCAD.

Figure 4.6 shows the positive voltage and current responses at the first ms after fault occurrence. V_{L1} shows the voltage at terminal L, which is the terminal close to the MMC rectifier. I_{L1} shows the corresponding current. V_{R1} and I_{R1} give the voltage and current responses on terminal R. This is the terminal between the overhead line and the sub-sea cable.
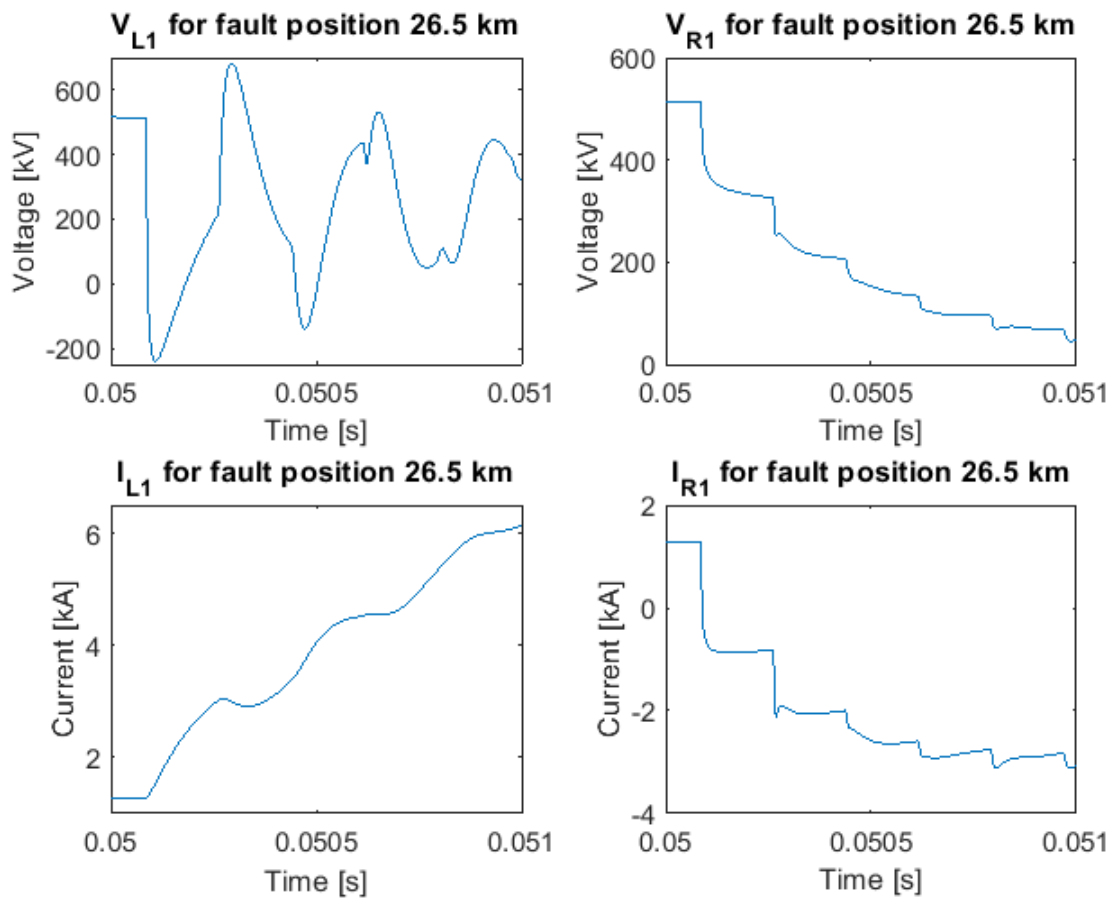
Figure 4.6: Positive pole voltage and current responses for a positive pole-to-ground fault occurring at 0.05 s for fault position 26.5 km

The current and voltage on terminal R are gradually decreasing during the first ms. On terminal L however, the voltage starts oscillating with large peaks before it begins stabilizing. The current at this terminal starts increasing with damped oscillations.

From each of these responses, detail coefficients were obtained. Figure 4.7 shows the coefficients of the positive pole voltages and currents at both terminals. Looking at the amplitudes, there is almost no change in the amplitudes of the current compared to the voltage. This would make it hard when determining thresholds for fault location. The detail coefficient of the voltage clearly shows the traveling waves as peaks with large amplitudes. The amplitude of the first incoming wave is approximately 250, while these decrease with more incoming waves due to power line losses and reflection losses. The peak behavior is different for the two terminals, where the detail coefficient peaks at terminal R are all positive in this case. A consequence of this observation was that only the voltage signals were used for the TWFL algorithms.
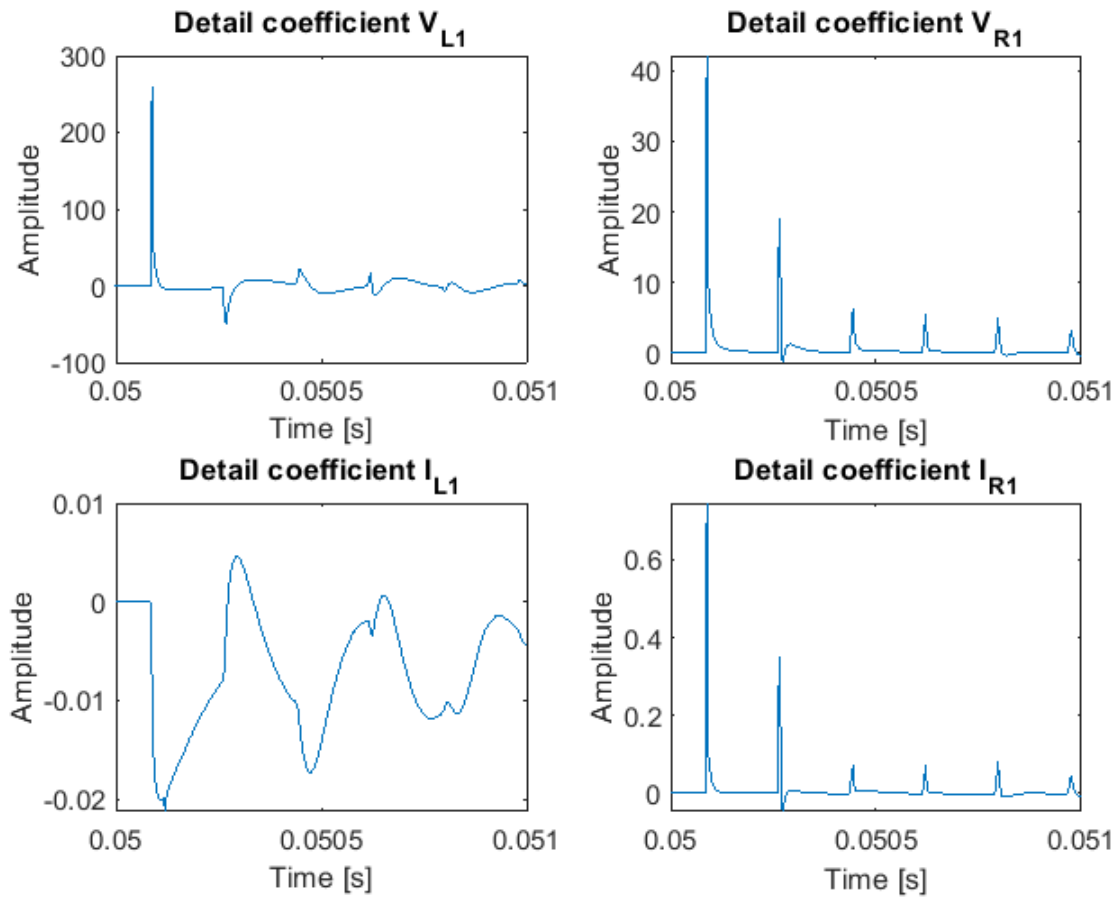
Figure 4.7: Detail coefficients for the positive pole voltages and currents for fault position 26.5 km

This observation also corresponds with a study saying that the wavelet coefficients of the voltage provide a better fault location than the coefficients using the current [80]. It is important to observe that the detail coefficient for the voltage on terminal R is relatively much lower than on terminal L.

4.2.2 Choosing TW propagation velocity

As described in Section 3.1, the wave propagation velocity is difficult to determine accurately as it varies with the type of fault, fault resistance, and fault location. The TWFL algorithms needed to implement wave velocity as a constant value for simplification of the algorithms. This simplification has also been conducted in other studies [63], [73]. In this case, the wave velocity was determined based on the test case above, a positive pole-to-ground fault in the middle of the line. The voltage on terminal L was used to find the first incoming TW. This is shown in Figure 4.8. This was the same voltage response V_{L1} as earlier for the first ms. By examining the first $100\,\mu s$ more closely, a visible change in the line graph can be seen at $t_1 = 0.05009 s$. The steepness of the line reduces at this point, indicating an incoming TW [59, p. 91].
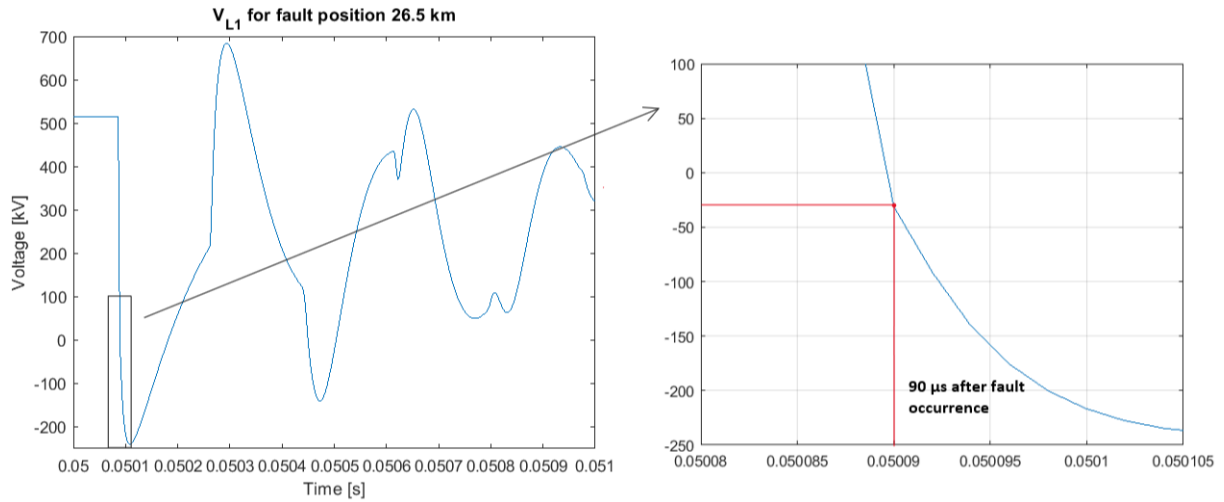
Figure 4.8: Obtaining first TW arrival time at terminal L. The change in line steepness is marked with a red dot at time $0.050\,09\,\mathrm{s}$

The red lines show at what voltage and what time this change occurred. By knowing the fault occurred at $0.05\,\mathrm{s}$, the time for the first traveling wave could be set to $t_{first,TW} = t1 - t_{fault} = 90\,\mu s$. Thus, the traveling wave propagation velocity was calculated in (4.2).

$$v = \frac{l_{fault}}{t_{first,TW}} = \frac{26.5\,\mathrm{km}}{90 \cdot 10^{-6}\mathrm{s}} = 294444.444\frac{\mathrm{km}}{\mathrm{s}} \tag{4.2}$$

The real speed of light is $299792.458\frac{\mathrm{km}}{\mathrm{s}}$ [5], which makes the calculated wave velocity equal to approximately 98.2% of the speed of light.

4.2.3 Choosing detail coefficient peak detection threshold

To prevent the algorithm from detecting false peaks, a detail coefficient peak detection threshold had to be determined. This value is difficult to calculate, therefore it was determined by looking at the test case. Because the voltage at terminal L had the highest peaks and is used for the single-ended fault location method, it was most relevant to determine the threshold based on this terminal.

Figure 4.9 shows the detail coefficients with the amplitude going from -50 to 50. This is to get a more detailed view of the boundary. The peak detection threshold value was set to ±10, to make sure that only the incoming waves were detected from a fault. The three first incoming waves are marked in the figure, which justifies the choice of the peak detection threshold. It would be expected that a fault further from the measurement terminal away will have smaller peaks, due to line propagation losses.
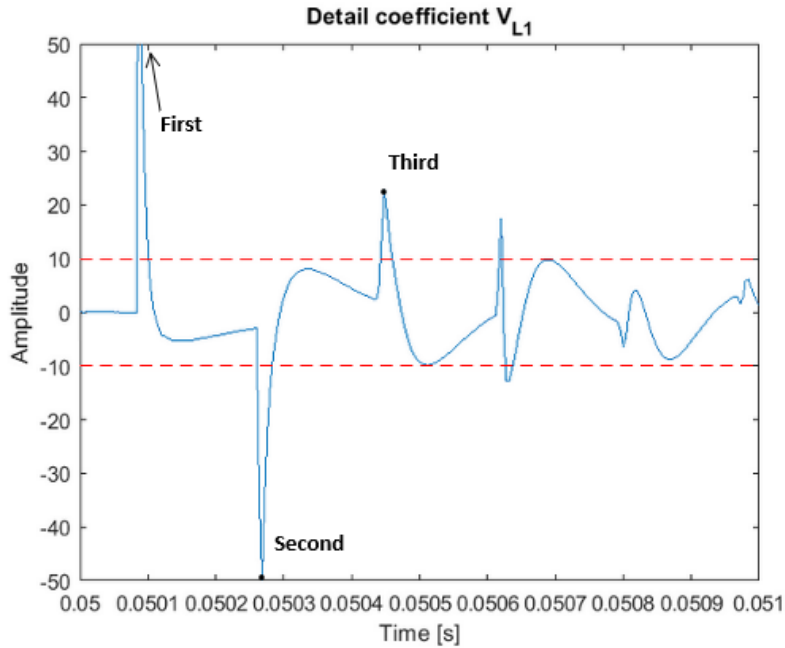
Figure 4.9: Boundaries for detail coefficient peak detection

4.2.4 Double-ended TWFL method

The double-ended TWFL method was the easiest to implement because only the first TW at each terminal was of interest. Figure 4.10 shows the procedure of the algorithm. The algorithm receives voltage signals from the terminals and uses the DWT Haar mother wavelet on level 1 to process the signals and obtain the detail coefficients. Further, the peaks above the peak detection threshold on both terminals are found. The first peak on both terminals is used for the fault calculation. The MATLAB functions used for this algorithm are given in Appendix C.

Voltage signals from
terminal L and R

DWT filtering

Threshold violation
check

No

No fault
located

Yes

First peak locations
t_L and t_R

$$loc_L = \frac{L_{line} - v(t_R - t_L)}{2}$$

$$loc_R = \frac{L_{line} + v(t_R - t_L)}{2}$$
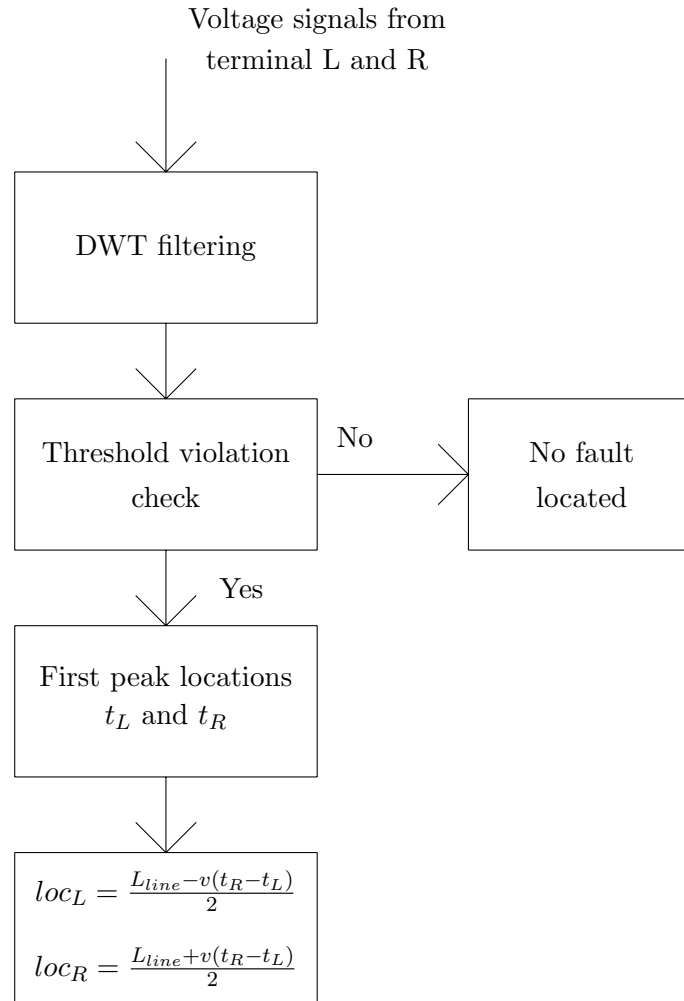
Figure 4.10: Double-ended TWFL algorithm

4.2.5   Single-ended TWFL method

There were two ways to implement the algorithm as already described in Section 3.4.2. The most accurate way was to use the arrival times of the three first traveling waves at the measuring terminal. This eliminates the wave velocity, which is difficult to determine accurately because it varies along the transmission line. The peak detection threshold was set in Figure 4.9, and it could be observed that the third wave had an amplitude of approximately 25, much lower than the two first peaks. It would therefore be a risk to use the three first waves, especially for faults further away from the measuring terminal. Therefore, the method using the two first waves was chosen.

As described in the Section 3.4.2, the single-ended method is more complicated compared to the double-ended method. This is due to the reason that the fault location has to be calculated in different ways depending on if the fault is located on the first or second half of the transmission line. The amplitudes of the detail coefficient are dependent on how far the waves have traveled and on their reflections.

It was necessary to determine if the second peak is reflected from the fault or from the opposite terminal. Therefore, the test case detail coefficient of the second incoming wave was used as a preference. The detail coefficient was shown in Figure 4.9. This amplitude had an absolute value close to 50. Faults further away from terminal L should be expected to have an absolute value lower than 50 due to increasing losses. Thus, the faults closer to the measuring terminal would be expected to have absolute values higher than 50. Therefore, a boundary was set to an absolute value of 50 to determine on which half the fault would be occurring. The algorithm procedure is given in Figure 4.11. The MATLAB functions used for this algorithm are given in Appendix C.
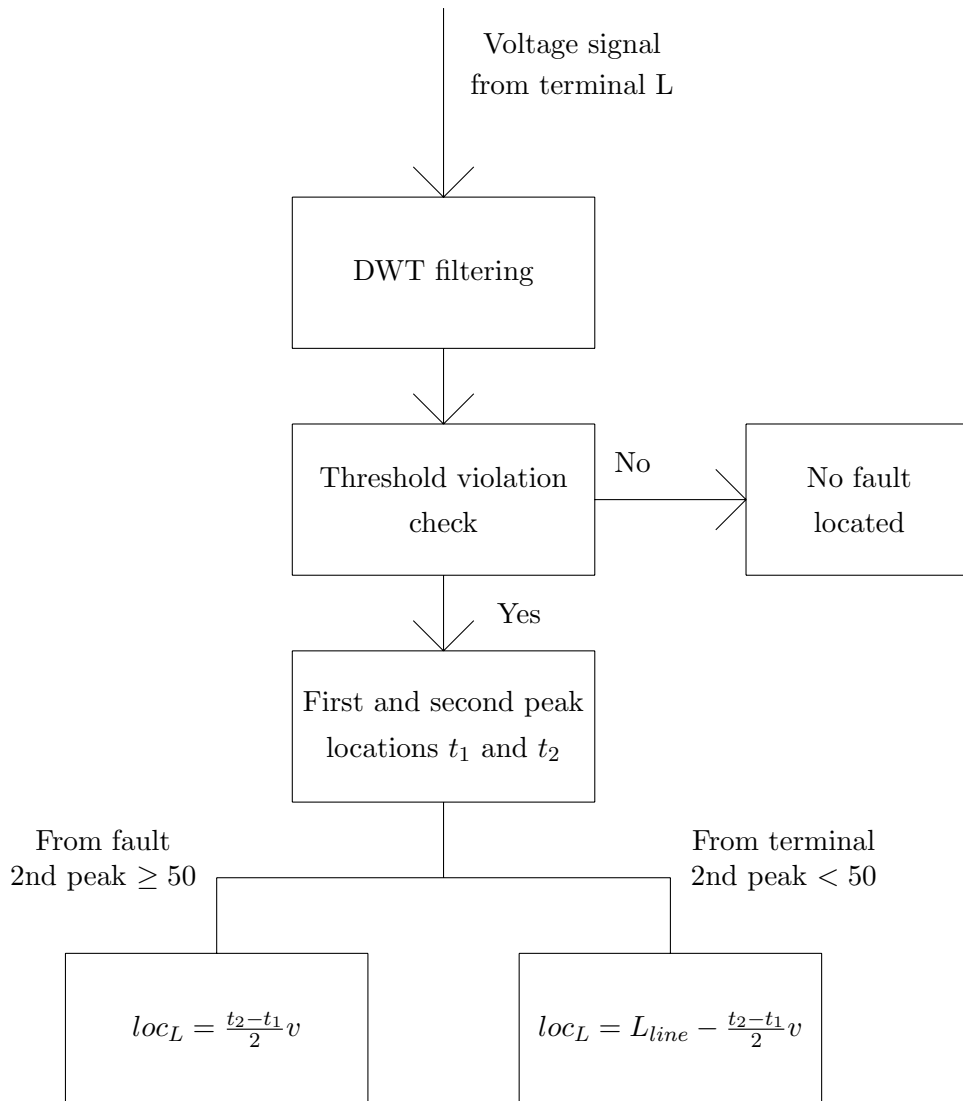
Figure 4.11: Single-ended TWFL algorithm

Chapter 5

Fault location results

This chapter contains the fault location results obtained from the double-ended and single-ended TWFL algorithms for the different simulation cases described in Section 4.1.3. The following sections are included in this chapter:

    5.1: Influence of fault position
    5.2: Influence of fault resistance
    5.3: Power system incidents
    5.4: MMC model VS. DC voltage source model

Each section gives all fault locations compared to the real fault positions applied in PSCAD. Errors were calculated based on (4.1). For cases where the fault location did not work, this is explained by showing the relevant detail coefficients. When investigating the influence of MMC on fault location, voltage responses and detail coefficients are included for comparison.

5.1 Influence of fault position

Seven different fault positions were applied at $0.05\,\mathrm{s}$ for a positive pole-to-ground fault with a fault resistance of $0.1\,\Omega$. Positions were given with reference to terminal L.

5.1.1 Double-ended TWFL

Table 5.1 shows the fault location results obtained by the double-ended TWFL algorithm. The algorithm correctly located all faults, with small errors in most cases. The largest error was $0.294\,\mathrm{km}$. Because the double-ended method uses the first incoming waves at both terminals, some of the tests gave similar results. Test 1 corresponds to 5 % of line length and test 7 corresponds to 95 % of line length. Thus, the error distance on $2.65\,\mathrm{km}$ was the same as for $50.35\,\mathrm{km}$, but with the opposite sign. This also yielded for test 2 and 6, and test 3 and 5.

Table 5.1: Double-ended fault location results corresponding to terminal L

Test	Real location [km]	Obtained location [km]	Error [km]	Error [%]
1	2.650	2.944	+0.294	+9.97
2	7.950	8.244	+0.294	+3.70
3	18.550	18.844	+0.294	+1.589
4	26.500	26.500	0.0	0.0
5	34.450	34.156	-0.294	-0.85
6	45.050	44.756	-0.294	-0.65
7	50.350	50.056	-0.294	-0.58

The error was almost 10 % for the fault closest to terminal L (test 1). This is a high percentage. Also, observe that the error distance was 0.294 km for the three first fault positions (test 1-3). 0.294 km corresponds to an error of approximately 1 μs.

5.1.2   Single-ended TWFL

Table 5.2 gives the fault location results of applying the single-ended TWFL algorithm. The absolute value of the error distance was in most cases 0.294 km, the same as when applying the double-ended TWFL algorithm. However, observe that the fault location failed for test 7. This is marked in red. The algorithm missed the real fault position by 46.817 km, which corresponds to an error of 93 %.

Table 5.2: Single-ended fault location results corresponding to terminal L

Test	Real location [km]	Obtained location [km]	Error [km]	Error [%]
1	2.650	2.944	+0.294	+9.97
2	7.950	7.656	-0.294	-3.70
3	18.550	18.256	-0.294	-1.589
4	26.500	26.500	0.0	0.0
5	34.450	34.744	+0.294	+0.85
6	45.050	44.344	-0.294	-0.65
7	50.350	3.533	-46.817	-92.98

To illustrate what went wrong in the fault location algorithm for the fault position of 50.35 km, the detail coefficient of the voltage on terminal L is shown in Figure 5.1.
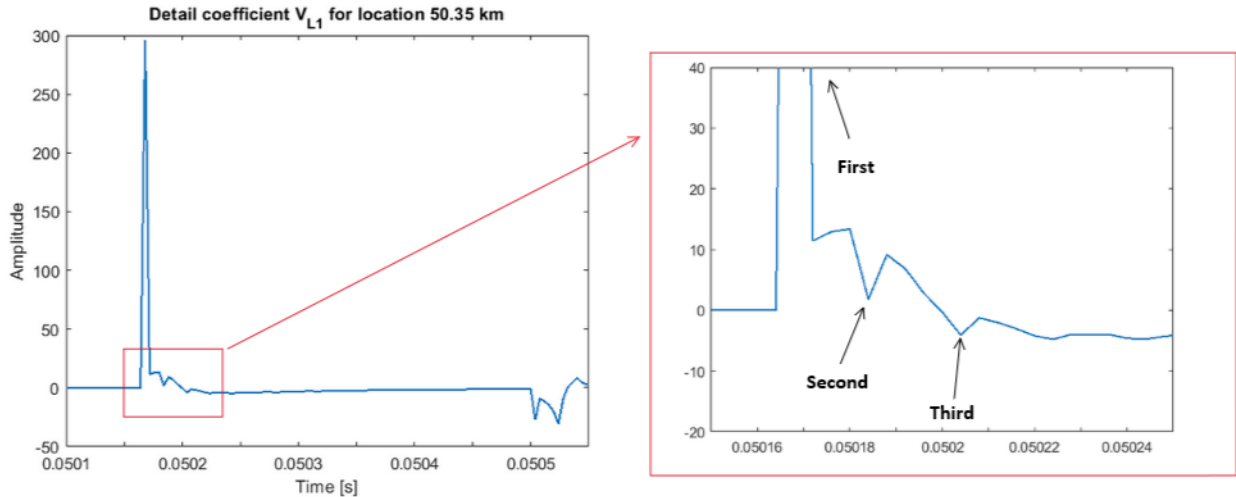
Figure 5.1: Detail coefficient for fault 50.35 km from terminal L

The first peak shows the first incoming wave with an arrival time of approximately 0.0517 s. The next incoming waves that should have been detected by the algorithms were the second and third waves marked in Figure 5.1. These peaks did not have an absolute peak value above the set threshold, thus they did not get detected. Because of this, the algorithm detected the peak occurring at around 0.0505 s as the second wave. Since it used the wrong peak, the fault location error was above 90%.

5.2   Influence of fault resistance

Changes in fault resistances were tested for 3 different locations, 18.55 km, 26.5 km and 34.45 km from terminal L. This was to test the resistance change for faults on both the first half and the second half of the HVDC overhead line. Table 5.3 gives the fault locations obtained from both the single-ended and double-ended TWFL algorithms for the different cases. In most cases, the fault locations were not affected by an increasing fault resistance. However, when using a fault resistance of 100 Ω there were two fault location failures. These cases are marked in red in the table.

Table 5.3: Fault location results for varying fault resistances

Fault position [km]	Fault resistance [Ω]	Single-ended [km]	Double-ended [km]
18.55	0.1	18.256	18.884
	10.0	18.256	18.844
	100	34.744	18.884
26.5	0.1	26.50	26.50
	10.0	26.50	26.50
	100	26.50	26.50
34.45	0.1	34.744	34.156
	10.0	34.744	34.156
	100	34.744	No fault located

For fault position 18.55 km, the single-ended algorithm located a 100 Ω fault resistance to 34.774 km. To further investigate this, the detail coefficient at 18.55 km is shown in Figure 5.2. The second peak has an amplitude of approximately 35. Thus, the algorithm determined the fault to be positioned on the second half of the line segment, corresponding to 34.774 km.
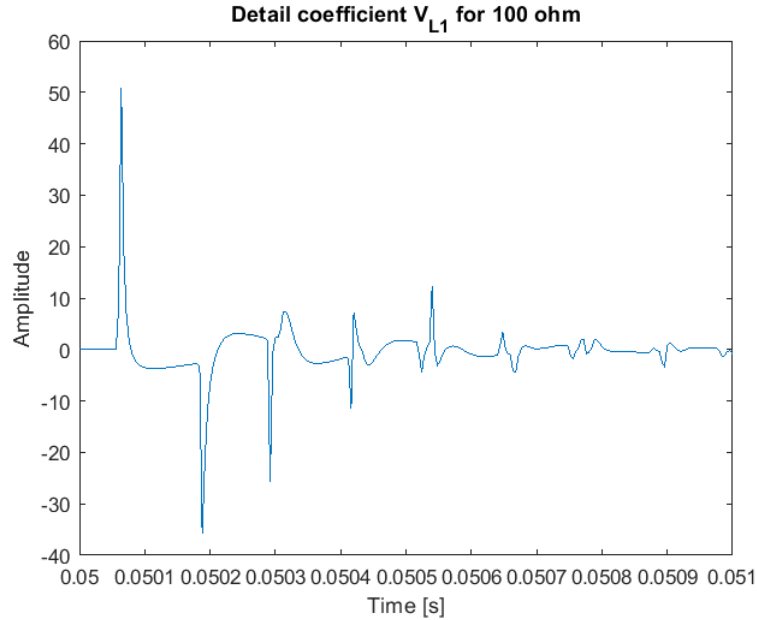
Figure 5.2: Detail coefficient on terminal L for 100 Ω at fault position 18.55 km

The second case where the fault location failed was for a fault position of 34.45 km and 100 Ω fault resistance. Figure 5.3 shows the detail coefficient at terminal R. With all detail coefficient peak values below the peak detection threshold of 10, no fault was located.
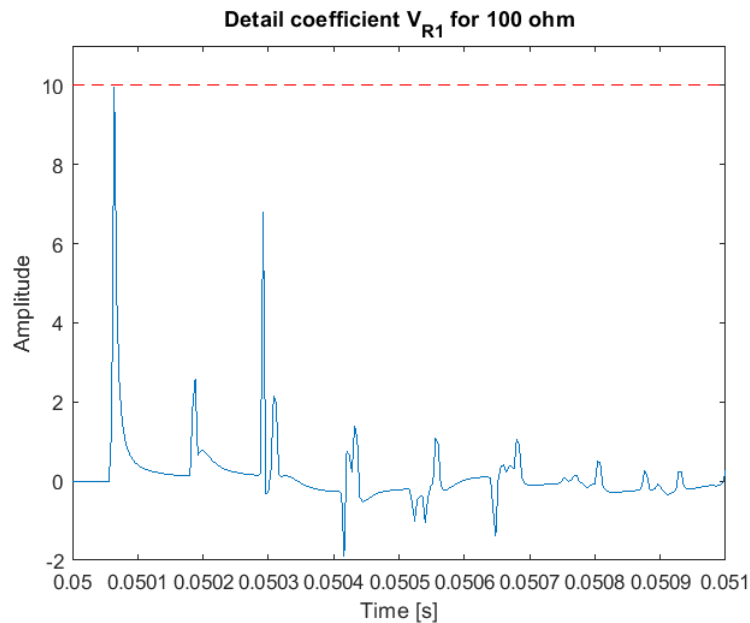
Figure 5.3: Detail coefficient on terminal R for 100 Ω at fault position 34.45 km

5.3   Power system incidents

Two types of power system incidents have been simulated. This is lightning strikes and AC grid disconnection. Two types of lightning strikes, on the ground wire and on the positive pole, were simulated on the overhead line for different amplitudes and locations. AC grid disconnection is a power system incident that does not give DC faults. This should therefore not be located by the TWFL algorithms as it is an incident outside the fault location zone.

5.3.1   Lightning strikes on ground wire

Lightning strikes on the ground wire were applied at fault positions of 18.55 km and 34.45 km. The current amplitudes simulated were 3 kA, 50 kA and 100 kA. Table 5.4 gives the fault location results from both the single-ended and double-ended TWFL algorithms.

Table 5.4: Fault location results for lightning strikes on ground wire

Fault position [km]	Amplitude [kA]	Single-ended [km]	Double-ended [km]
	3	No fault located	No fault located
18.55	50	0.589	18.844
	100	0.589	18.844
	3	No fault located	No fault located
34.45	50	51.822	34.156
	100	1.178	34.156

Based on the results above, Table 5.5 gives the errors of each fault location in %.

Table 5.5: Fault location errors for lightning strikes on ground wire

Fault location [km]	Amplitude [kA]	Single-ended [%]	Double-ended [%]
	3	No fault located	No fault located
18.55	50	-96.82	1.58
	100	-96.82	1.58
	3	No fault located	No fault located
34.45	50	50.43	-0.85
	100	-96.58	-0.85

Observe that current amplitudes of 3 kA did not give fault location. For amplitudes of 50 kA and 100 kA the double-ended algorithm located the fault to be at 18.844 km. The algorithm did also correctly locate the fault on 34.45 km. The main issue is the results obtained by the single-ended algorithm. No fault locations were correct. The reason for this can be observed in Figure 5.4, showing the detail coefficients for the different strike amplitudes. Each incoming wave gave both a positive and a negative peak. This made the single-ended wave detect both peaks of the same wave to calculate the fault, thus giving wrong fault locations.
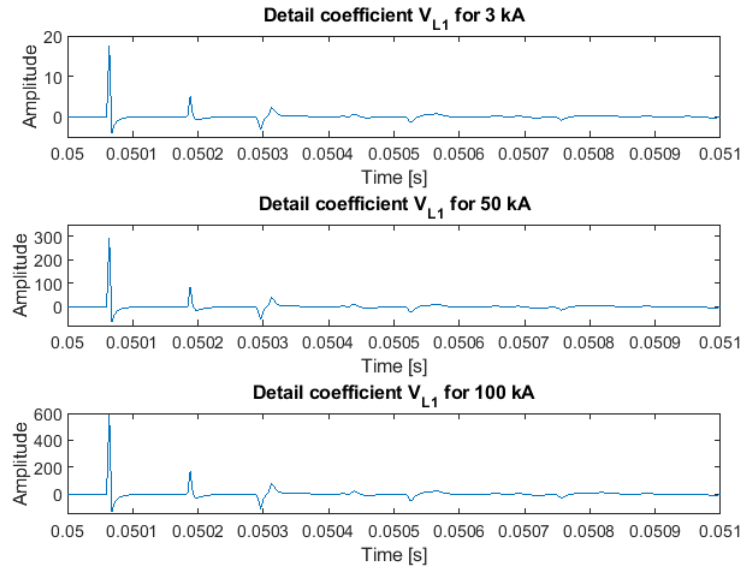
Figure 5.4: Detail coefficients for different lightning strike currents at terminal L for a fault occurring at 18.55 km

An amplitude of 3 kA did not give any fault location because the only detail coefficient peak above the peak detection threshold of 10 was the first peak at terminal L. The algorithms need two peaks for fault location. Observe the low detail coefficients in Figure 5.5.
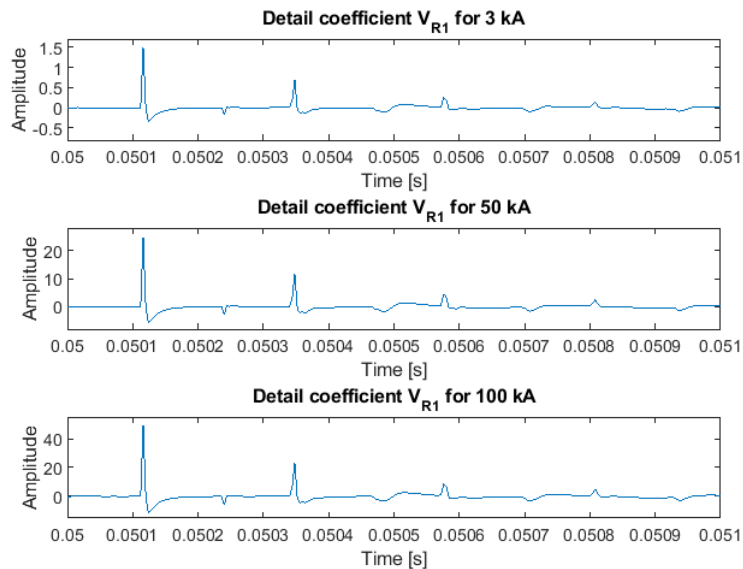
Figure 5.5: Detail coefficients for different lightning strike currents at terminal R for a fault occurring at 18.55 km

5.3.2 Lightning strikes with shielding failure

Shielding failure was tested by applying the lightning current directly on the positive pole. The fault location results are shown in Table 5.6. Observe the double-ended algorithm correctly located all faults within a reasonable error.

Table 5.6: Fault location results for lightning strikes with shielding failure

Fault position [km]	Amplitude [kA]	Single-ended [km]	Double-ended [km]
	3	0.589	18.844
18.55	10	0.589	18.844
	3	51.822	34.156
34.45	10	1.178	34.156

Based on the results above, Table 5.7 gives the errors of each fault location in %.

Table 5.7: Fault location errors for lightning strikes with shielding failure

Fault position [km]	Amplitude [kA]	Single-ended [%]	Double-ended [%]
	3	-96.82	1.58
18.55	10	-96.82	1.58
	3	50.43	-0.85
34.45	10	-96.58	-0.85

The single-ended method, however, did not locate the faults correctly. Figure 5.6 shows the detail coefficient peaks on terminal L for the fault occurring at 18.55 km. Like for lightning strikes on the ground wire, the first wave had both a positive and negative peak. Even though the positive peak, in this case, was much more damped, the single-ended algorithm still detected both peaks from the first wave and used these for the fault location.
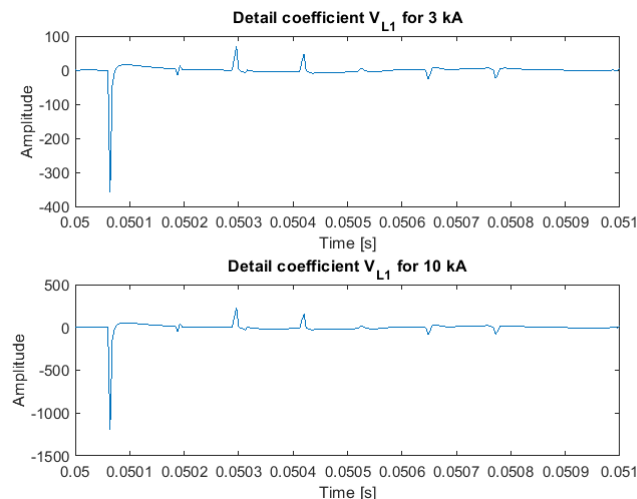
Figure 5.6: Detail coefficients at terminal L for lightning strikes with shielding failure for fault position 18.55 km

5.3.3   AC grid disconnection

Lastly, an AC grid disconnection was simulated. The CB located in the 420 kV AC grid was opened at 0.05 s. Both the single-ended and the double-ended TWFL algorithms gave "No fault located". This means that the algorithms saw no possible fault in the system based on the fault location boundaries that had been given. The voltage responses and detail coefficients for both terminals can be found in Appendix D.

5.4   MMC model VS. DC voltage source model

A simplified model of the HVDC transmission system was made utilizing DC voltage sources. The goal was to test if it was possible to simplify the power system model to reduce the computational time, to obtain a better sampling rate, and still get the same results. Two fault positions were used, 18.55 km and 34.45 km. Only the voltage responses of a fault at 18.55 km are shown in this section. The responses of the fault at 34.45 km are given in Appendix D. When comparing the models, both voltage responses and detail coefficients were used to investigate how the different models reacted during the fault. The fault resistance used was 0.1 Ω. For this comparison, only sampling times of 2 μs were used. When obtaining the fault location results, however, also 1 μs was used for the DC voltage source model.

5.4.1   Comparison of voltage responses

Figure 5.8 shows the MMC and DC voltage source model responses at terminal L. The two voltage responses both oscillated in the same way but stabilized on different voltage levels after some time. By looking at the more detailed response in Figure 5.7b, it can be observed that the oscillations of the DC voltage source model got more phase shifted with an increase in time.
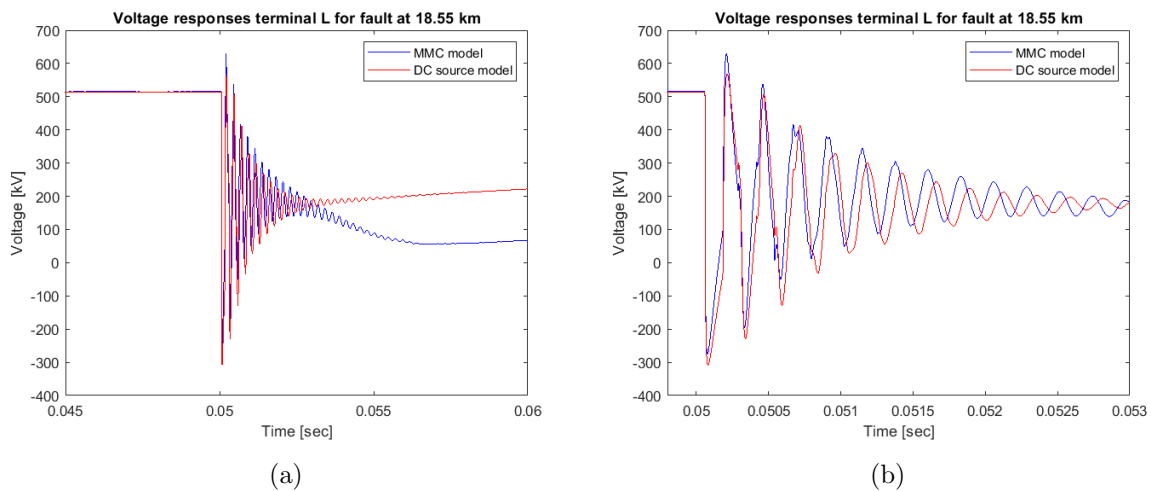
Figure 5.7: Positive pole voltage responses at terminal L for HVDC-MMC model and DC voltage source model at fault position 18.55 km, (b) gives a more detailed look at the first oscillations.

For the responses on terminal R, the models were even more similar during the first 3 ms as seen in Figure 5.8b. However, the voltage stabilized on different levels after some time. This is shown in Figure 5.8a. There was no clear phase shift for this terminal compared to terminal L.

(a)   (b)
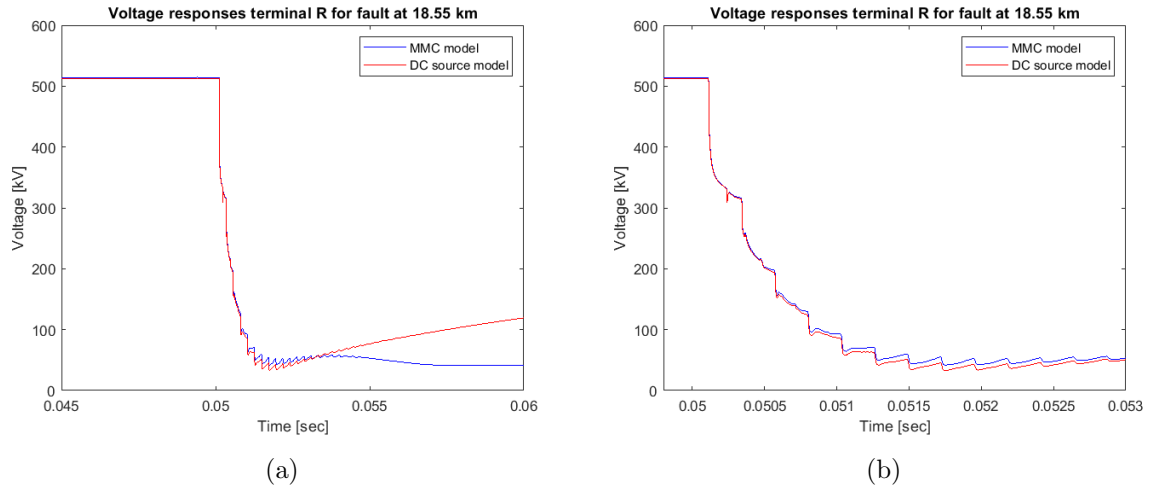
Figure 5.8: Positive pole voltage responses at terminal R for HVDC-MMC model and DC voltage source model at fault position 18.55 km, (b) gives a more detailed view of the response.

5.4.2 Comparison of detail coefficients

Further, looking at the detail coefficients in Figure 5.9, it is difficult to physically observe any large differences in the peak amplitudes and in their locations.

(a) Terminal L   (b) Terminal R
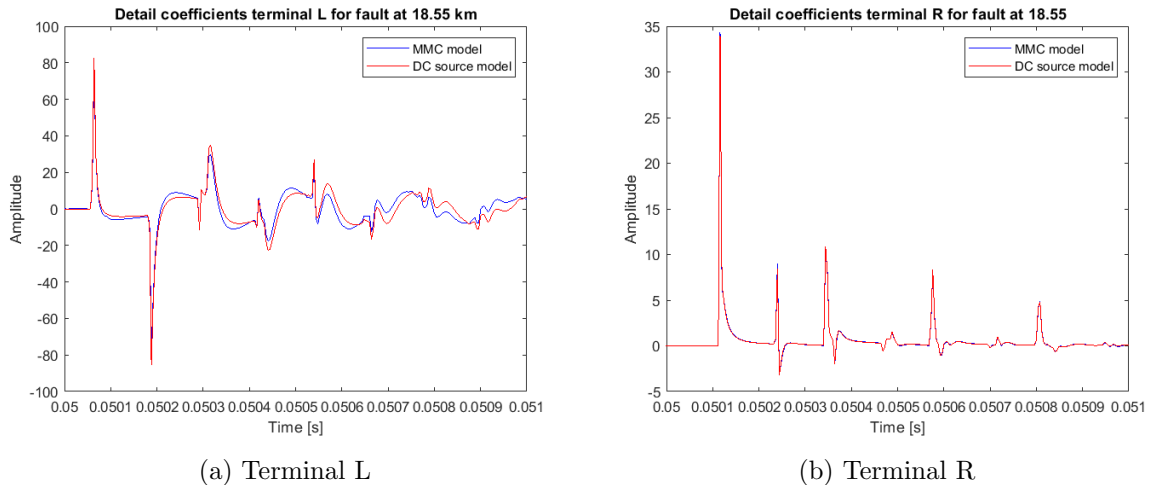
Figure 5.9: Detail coefficients for HVDC-MMC model and DC voltage source model at fault position 18.55 km.

To search for any difference in the amplitudes for the first and second peaks, their values were obtained in MATLAB. The complete table with all detail coefficient peaks is given in Table D.3. When comparing the HVDC-MMC model to the DC source model with the same sampling rate, the following values were obtained for 18.55 km:

- First wave at terminal L had peak values of 77.3 for the MMC model and 82.5 for the DC source model.

- Second wave at terminal L had peak values of -76.8 for the MMC model and -85.6 for the DC source model.

- First wave at terminal R had peak values of 34.3 for the MMC model and 34.0 for the DC source model.

This shows that the peak values correspond quite well between the models.

5.4.3   Fault location results

Table 5.8 shows the fault location results by comparing the MMC model with a sampling rate of 2 µs with the DC source models with sampling rates of 2 µs and 1 µs. This was for a fault position of 18.55 km.

Table 5.8: Comparison between the MMC model and the DC source model using sampling times of 2 µs and 1 µs at fault location of 18.55 km

	MMC model (2 µs)	DC source model (2 µs)	DC source model (1 µs)
Double-ended	18.844 km	18.844 km	No fault located
Single-ended	18.256 km	18.256 km	34.744 km

With sampling rates of 2 µs, the algorithms obtained the same fault locations for the MMC model and the DC source model. With the DC source model and 1 µs sampling time, however, the fault location failed for both algorithms. The detail coefficient values provided in Table D.3 show why this happened. The double-ended method did not locate the fault because the first peak on terminal R had a value of 9.01, below the peak detection threshold. The single-ended method did not locate the fault correctly because the value of the second peak on terminal L had an absolute value below 50, making the algorithm determine the fault to be on the second half of the line.

By looking at the fault at 34.45 km, Table 5.9 shows few differences between the three models. The double-ended method gave a more accurate fault location when using signals from the DC source model with sampling time 1 µs.

Table 5.9: Comparison between the MMC model and the DC source model using sampling times of 2 µs and 1 µs at fault location of 34.45 km

	MMC model (2 µs)	DC source model (2 µs)	DC source model (1 µs)
Double-ended	34.156	34.156	34.450
Single-ended	34.744	34.744	34.744

Chapter 6

Chapter 6

Discussion around factors affecting fault location accuracy

In Chapter 5, the fault location results were based on the wavelet detail coefficient peak values and their locations in time. Several factors could have affected the results obtained by the TWFL algorithms. These factors will be further discussed in this chapter, and the single-ended and double-ended TWFL algorithms will be compared. The following sections are included:

    6.1: Influence of fault position on detail coefficients
    6.2: Influence of fault resistance on detail coefficients
    6.3: Fault location challenges for lightning strikes
    6.4: Discussion around different modeling approaches
    6.5: Other factors affecting fault location accuracy
    6.6: Closing remarks on single-ended and double-ended TWFL

6.1 Influence of fault position on detail coefficients

When developing the single-ended TWFL algorithm in Section 4.2.5, it was assumed that the values of the detail coefficient peaks of the positive pole voltage would be reduced for an increasing fault distance. This is because a fault far away would be expected to be affected by larger line losses and larger differences in the arrivals of the TW frequency components. Thus, the voltage response would be more damped, making the detail coefficient peaks smaller compared to a fault closer to the measuring terminal. To further analyze this, graphs are made to illustrate how the detail coefficient peaks vary with the fault position at both terminals. A table with all peak values used in these comparisons is available in Table D.1. The peaks of the first incoming wave at terminal L and R are given in Figure 6.1. The red dashed lines show the peak detection threshold set at ± 10.

(a) Terminal L
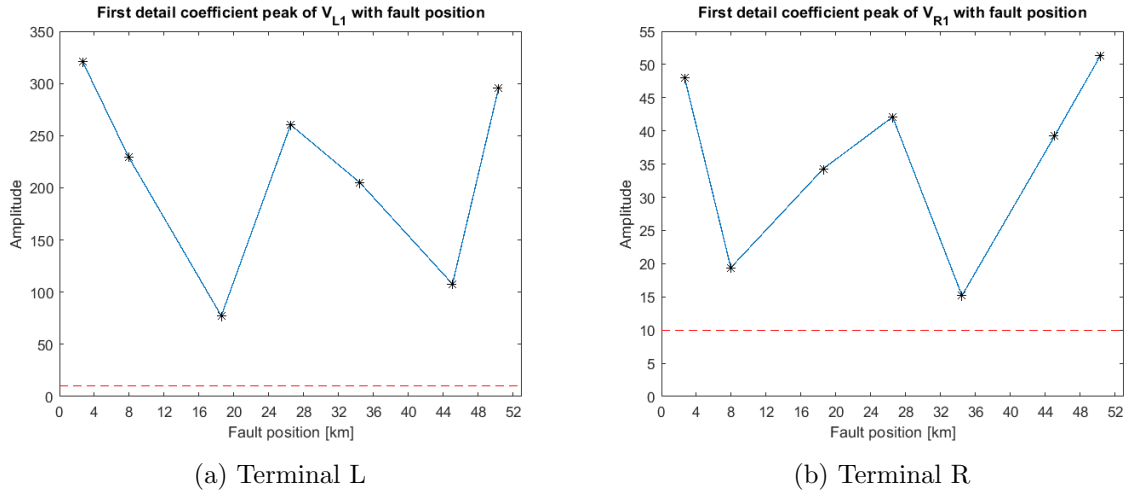
(b) Terminal R

Figure 6.1: Influence of fault position on detail coefficient peaks on terminal L and R

For both terminals, it does not seem to be a correspondence between the detail coefficient peak values and an increasing fault position. In Figure 6.1a the position of 18.55 km gives a low peak value, and for 26.5 km and 50.35 km the values are high. The same pattern can be observed for terminal R in Figure 6.1b. It can therefore not be proven that a higher fault distance gives a smaller detail coefficient peak for the first incoming wave.

Figure 6.2, on the other hand, shows a correspondence between the peak value of the second incoming wave and the fault position. The dashed blue line is positioned at an amplitude of -50 and shows the boundary of whether the fault is located on the first half or the second half of the overhead line. The total overhead line length is 53 km.
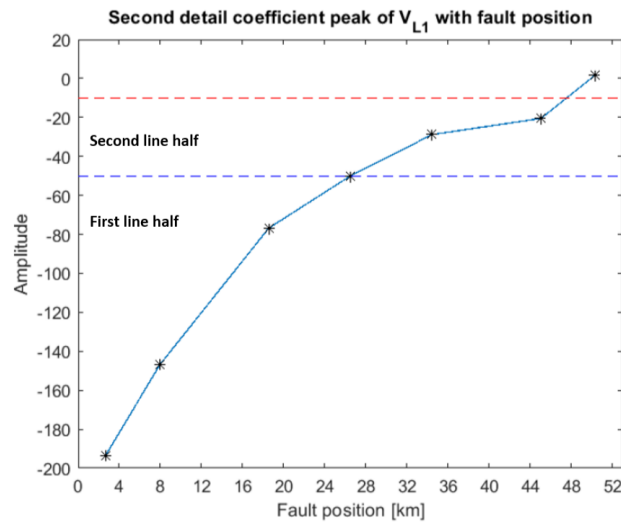
Figure 6.2: Influence of fault position on second detail coefficient peak on terminal L

Observe that the fault occurring at 50.35 km has a peak value above the threshold of -10 and is outside the boundary of peak detection. This fault position did not get located correctly with the single-ended TWFL algorithm.

One can use the arrival of the frequency components of each wave as a possible reason for this result. The first wave does not have enough time to stop completely before the second incoming wave is measured at the terminal. It can be seen as the highest frequency component of the second incoming wave catching up with the lowest frequency components of the first wave. Because of this, the second wave is not starting at zero amplitude, but at around 10, as it was shown in Figure 5.1. This is an issue for faults close to the terminals as the TWs consist of different frequency components propagating at different speeds. This problem is thus only affecting the single-ended TWFL algorithm.

The sampling rate can be one reason for the lack of correspondence between the first peaks and the fault positions. It was stated in Section 3.2.1 that a sampling rate of at least 1 MHz is necessary to properly detect incoming TWs, however, the voltage was measured with a sampling rate of 500 kHz. By further using DWT, the sampling rate was halved to 250 kHz. Using CWT could therefore have given more accurate peak values for the first peaks. Because the first peak had strange values for the different positions, it is also necessary to question why the second incoming wave gave peaks that were decreasing with increasing fault positions. In this case, the waves have been subject to line losses and reflection losses. This is decreasing the wave velocity and amplitude. Thus, the need for a high sampling rate is not as important for the second wave as it is for the first wave.

6.2 Influence of fault resistance on detail coefficients

For the discussed fault positions, the fault resistance was $0.1\,\Omega$, which is a fault resistance that does usually not cause major issues for the fault location algorithms. It has earlier been mentioned in Section 3.3 that high-impedance faults are said to be difficult to detect correctly, and this can be confirmed by looking at the fault location results for $100\,\Omega$ fault resistances. To further analyze the influence of fault resistance, the detail coefficients of the first incoming wave at terminal L and R are given in Figure 6.3.

(a) Terminal L   (b) Terminal R
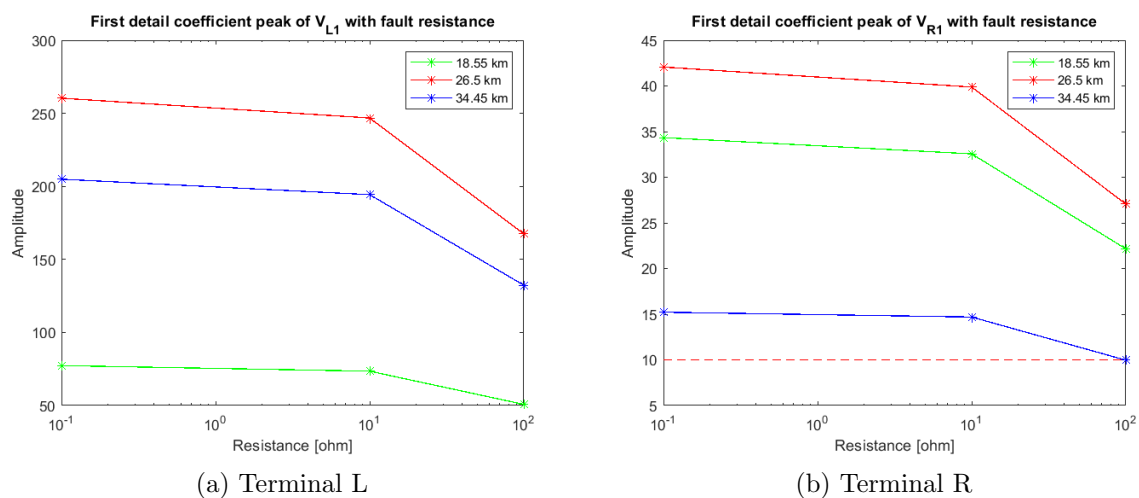
Figure 6.3: Influence of fault resistance on first detail coefficient peaks on terminal L and R for three different fault positions

The figure shows that an increase from $0.1\,\Omega$ to $10\,\Omega$ gives a significantly smaller change in detail coefficient peak values compared to an increase from $10\,\Omega$ to $100\,\Omega$. This yields for both terminals. The double-ended method is vulnerable to high-impedance faults due to the peak values given in Figure 6.3b.

It should be expected that the absolute values of the second peaks will also behave in a similar wave for an increasing fault resistance as the first peaks.
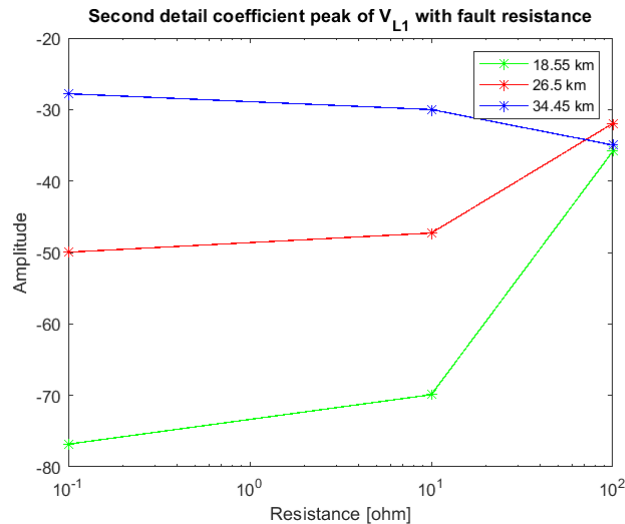
Figure 6.4: Influence of fault resistance on second detail coefficient peak on terminal L for three different fault positions

This is correct for the fault positions of $18.55\,\mathrm{km}$ and $26.5\,\mathrm{km}$. However, for the position on the second half of the overhead line, the absolute value of the detail coefficient peak increases with an increased fault resistance. This seems strange, as the resistance will lead to more damped voltage responses, thus also a decrease of detail coefficient values. Further investigation of the second incoming peak for fault positions on the second half of the transmission line is necessary to conduct to look for similar results.

6.3   Fault location challenges for lightning strikes

As seen in the Section 5.3, the single-ended TWFL algorithm failed to locate the fault positions of all applied lightning strikes. The reason for this was that each incoming wave gave both a positive and negative peak, confusing the algorithm to believe there were two incoming waves almost at the same time. The algorithms were developed based on the behavior of pole-to-ground faults, and it was assumed that lightning strikes would give the same behavior for the detail coefficients. However, the behavior of lightning strikes did not correspond to the behavior of single pole-to-ground faults. This observation makes the single-ended algorithm vulnerable. The double-ended method, however, is not affected by this observation.As lightning strikes are very common to occur, this is an important challenge to investigate.

To overcome this single-ended fault location problem, a different wavelet strategy can be investigated. It is important that the mother wavelet, which is moved along the time-axis of the signal, corresponds to the signal that is analyzed. The Haar mother wavelet may not be the best-suited wavelet for handling lightning strikes. In Section 3.2.2, it was specifically stated that the Haar wavelet is good at detecting the first incoming wave, with the wavelet being a step function. Thus, there might be other wavelets better to separate the incoming waves from each other, as the choice of wavelet type influences the shape of the detail coefficients. Using CWT could also be a better choice as this transform is said to be more accurate. However, it is important to use a function that suits all possible incidents in a transmission system. Another way to overcome this problem can be to investigate the use of a combination of voltage and current measurements to determine if a wave has been detected, such as the novel method proposed in Section 3.4.4 [80].

6.4   Discussion around different modeling approaches

The MMC model was compared to the DC source model using a sampling time of 2 µs. This resulted in the same fault locations, even though the detail coefficient peak values were slightly changed. However, for a longer time perspective, the voltages stabilized on different voltage levels and the signals got more phase-shifted with time until the oscillations were gone. A reason for this difference between the two models is the MMC control functions explained in Section 2.2. The MMC control principles cannot be achieved by only utilizing DC voltage source models. Consequently, the voltage response of the simplified model is considered less realistic.

Phase-shifted signals also make the detail coefficient peaks phase-shifted. Thus, the time arrivals of the waves will not correspond between the models. However, it can be discussed how long time perspective is needed after the first incoming wave for fault location based on TWs. This is dependent on the different cases. In this system, the total overhead line length is only 53 km, meaning that a wave only needs approximately 180 µs to propagate along the entire line. For very long transmission lines, such as in Brazil [5], a line length of 2300 km corresponds to a transmission line propagation time of almost 8 ms. However, the proposed algorithms only require two waves, and it would not have made a significant difference, in this case, to use the DC source model with a sampling time of 2 µs. Because the voltage is not phase-shifted until after some time, the simple model can be a good choice in this specific case with a short line length.

By changing the sampling time of the DC source model to 1 µs, one would expect more accurate fault location results. This model gives a more accurate result for the fault at 34.45 km, however, the algorithms are not able to correctly locate the faults occurring at 18.55 km. By only using two different fault positions, it cannot be concluded that a lower sampling time results in better fault location accuracy in this case. To properly determine this, different types of studies should be conducted. It is also important that the TWFL algorithms were developed for a pole-to-ground fault with a sampling time of 2 µs. A lower rate could give different peak values, and the thresholds used in the algorithms should in that case be adjusted to the new model.

It can be argued that the double-ended method will be least affected by using a simplified model. The only critical point for this algorithm is the detail coefficient peaks on terminal R, as these are significantly lower than on terminal L.

6.5   Other factors affecting fault location accuracy

6.5.1   Sampling rate

The sampling time used in the MMC model has been used as a possible reason for the strange detail coefficient values of the first incoming wave at terminal L and R. In Section 3.2.1, it was stated that a sampling rate of minimum 1 MHz is necessary to accurately detect TWs. Unfortunately, the MMC model could only handle a sampling rate of 500 kHz, which makes the signal from PSCAD only sample every second µs. By applying the DWT and wavelet coefficients at level 1, the detail coefficients detect waves with twice as high sampling time compared to the incoming signal. Thus, TWs are detected with a sampling time of 4 µs. This way, the algorithm can miss the incoming wave with a maximum of 3 µs. This corresponds to fault location error of by $3\,\mu s \cdot 294.4\,\frac{m}{\mu s} = 883\,m$. $294.4\,\frac{m}{\mu s}$ is the wave velocity found in Section 4.2.2. This maximum error is large for a fault very close to the measuring terminal and will give the impression of poor fault location algorithms. By using CWT instead, it would be possible to locate the fault with a sampling time equal to the MMC model, this would also make the errors much smaller.

6.5.2   Hybrid transmission lines

When using an HVDC system with hybrid transmission lines, this can influence the fault location accuracy. Even though the measuring terminals are placed on either side of the overhead line, the cable near terminal R affects the fault responses. In Section 2.4, it was stated that cables are highly capacitive. This capability can be observed in the results, by significantly smaller detail coefficient peaks on terminal R. The voltage changes are more smooth, thus the oscillations are more damped compared to terminal L. This was earlier discussed when looking at varying fault positions and fault resistances. Due to the peaks of the detail coefficient being so low for the first incoming wave at terminal R, it would probably be a bad idea to use a terminal like this for the implementation of a single-ended TWFL algorithm. If one would implement such an algorithm between an overhead line and a cable, the threshold would need to be lower to properly detect the incoming waves. Because the cable is suppressing rapid voltage changes, one could also argue that it would be easy to implement a single-ended location algorithm on terminal R because the noise of the signal will be smaller and this could make sure that no false waves are detected. There are also no large negative peaks, which will make the algorithm easier as it only needs to detect the positive peaks. Even though terminals on both converter ends were used for fault location in [4], [78], this was not considered in this work because the cable length is above 500 km and the velocity is slower in the cable compared to the overhead line.

6.6   Closing remarks on single-ended and double-ended TWFL

The results clearly show that the double-ended method obtains the best fault location results. When applying different fault positions and different fault resistances, this algorithm usually managed to locate the fault. Only high-impedance faults lead to fault location failure for both single-ended and double-ended algorithms. The double-ended method also located all lighting strikes correctly, which was a major issue for the single-ended algorithm. This method was especially vulnerable to lightning strike scenarios because of the shape of the detail coefficients. This indicates that double-ended TWFL would be safer to utilize.

The hybrid transmission line may have contributed to fault location issues for high-impedance faults when using the double-ended method. It is possible to argue for having a lower threshold on terminal R to be able to detect all incoming waves. The threshold was set to 10 to make sure that only real incoming TWs at terminal L were detected. However, terminal R is subject to the capacitive cable segment, suppressing large voltage changes. This contributed to making the detail coefficients smaller, also with less noise and few false peaks. It can therefore be possible to adjust the peak detection threshold at terminal R and make the double-ended method less vulnerable to high-impedance faults.

It would be preferred to use both voltages and currents for the fault location for the single-ended TWFL algorithm. This method lacks a good way to distinguish between faults occurring on the first half and second half of the transmission line. This issue is also discussed in Section 3.4.2 as the main challenge when using single-ended methods.

There is, in real power systems, a certain time delay between the measurement devices for double-ended methods. In PSCAD, this is not visible, thus it does not necessarily give the most realistic results compared to real applications. However, this time delay is not large and would only affect the fault location results to a small degree. The single-ended method, on the other hand, does not have this issue as there is no need for time synchronization between devices. The proposed method, however, has several issues which make the double-ended method a better choice even though the method requires more equipment and larger overall costs. The only difference between the single-ended and double-ended methods are the number of measuring devices. It can therefore be expected that the double-ended TWFL method should work in single-ended method mode if one of the devices gets damaged. This makes the fault location system reliable, which is stated in Chapter 3 to be an important factor when implementing protection and fault location systems.

Chapter 7

Conclusion

The purpose of this thesis has been to investigate TWFL on HVDC-MMC transmission lines, and how the fault location accuracy can be affected by different system parameters or modeling approaches. Positive pole-to-ground faults were applied with varying fault positions and fault resistances. The single-ended and double-ended TWFL algorithms located the faults within a reasonable error in most cases. However, for a fault close to the opposite terminal, the single-ended method had a fault location error of nearly 93 %. It was observed that an increasing fault distance with reference to terminal L, corresponded to the decrease of the detail coefficient peaks for the second incoming wave. This resulted in a fault location failure by the single-ended algorithm for a fault at 95 % of the overhead line length, where the real second incoming wave was not detected correctly. The first incoming wave on both terminals did not have detail coefficient peaks that seem to correspond to the fault position applied. This can be influenced by using a sampling rate below the recommended sampling rate level.

The occurrences of high-impedance faults were more difficult to locate as the peaks of the detail coefficients were heavily decreased compared to low-impedance faults. At 34.45 km from terminal L, the fault could not be located with the double-ended method. It can be concluded that high-impedance faults are more challenging as the voltage responses are more damped, which can contribute to peak values below the peak detection threshold. This is also an issue for the single-ended TWFL algorithm.

When applying power system incidents to the system, AC grid disconnection did as expected not give fault location, because the detail coefficients were below the peak detection threshold. However, when applying lightning strikes, the single-ended method did have issues for all cases. The reason for this was that each incoming wave resulted in both a positive and negative peak. Only the double-ended method did correctly locate all lightning strikes. This is a severe disadvantage of the single-ended algorithm, as one can never know exactly what kind of faults will occur on an HVDC overhead line. A strategy to overcome this problem is by using another wavelet approach, either by using CWT, or DWT with other mother wavelets. It is also possible to investigate the use of both currents and voltages for fault location.

By comparing the HVDC-MMC model to a simplified model using DC voltage sources on both ends of the transmission line, the fault location results were not affected for a sampling time of 2 µs. The fault location algorithms only need the two first incoming waves, and therefore it can be concluded that the DC voltage source model is a good choice for this sampling rate. However, a sampling time of 1 µs for the DC source model led to fault location failure for one of the fault positions. It cannot be concluded if using the DC source with a lower sampling time is the best choice in this work because the algorithms are based on the MMC model with 2 µs sampling time.

To conclude this work, the double-ended TWFL algorithm obtained the best fault location results. It did locate almost all faults correctly, however, high-impedance faults and faults very close to the opposite terminal are challenging, as the fault responses are more damped. This algorithm also located lightning strikes within a reasonable error, which the single-ended algorithm did not manage. Even though the double-ended method requires time synchronization and has higher overall costs, this method is concluded to be the most reliable fault location method.

7.1   Further work

This thesis has shown the advantages and disadvantages of the proposed TWFL methods. It has investigated how different system parameters and modeling approaches affect fault location accuracy, and there are several opportunities for further work on this topic. Some examples are given below:

- Faults can be applied on the sub-sea cable to investigate how an external fault from the cable affects the TWFL algorithms. The algorithms should be able to differ between internal and external faults occurring on the hybrid transmission line.

- It is more difficult to use single-ended TWFL for a transmission line consisting of several segments of overhead lines and cables. This is because the TWs get reflected at discontinuities on the line, such as the boundary between the overhead lines and cables. It would be interesting to study how lines consisting of several line segments affect the fault location accuracy.

- Using other types of wavelet approaches was a possible strategy to manage to locate lightning strikes with the single-ended method. Therefore, different types of mother wavelets should be investigated to understand how this influences the fault location.

- A simplified model based on DC voltage sources was made to manage to use smaller sampling times for better fault detection. This should be further investigated for different types of faults and using different types of transmission system models.

- A more specific investigation of the effect of VSC hybrid transmission lines on TWFL can be done. This is a field that is not so much researched. Faults on a hybrid transmission line should be compared to faults on a transmission line with only one line segment.

References

[1] M. Callavik, P. Lundberg and O. Hansson, 'NORDLINK Pioneering VSC-HVDC interconnector between Norway and Germany', *A White Paper from ABB*, 2015.

[2] G. Andersson and M. Hyttinen, 'Skagerrak: The Next Generation: HVDC and Power Electronic Technology System Development and Economics', 2015.

[3] L. Harnefors, A. Antonopoulos, S. Norrga, L. Angquist and H.-P. Nee, 'Dynamic Analysis of Modular Multilevel Converters', *IEEE Transactions on Industrial Electronics*, vol. 60, no. 7, pp. 2526–2537, 2013. DOI: 10.1109/TIE.2012.2194974.

[4] H. A. Al Hassan, B. M. Grainger, T. E. McDermott and G. F. Reed, 'Fault Location Identification of a Hybrid HVDC-VSC System Containing Cable and Overhead line Segments Using Transient Data', in *2016 IEEE/PES Transmission and Distribution Conference and Exposition (TD)*, 2016, pp. 1–5. DOI: 10.1109/TDC.2016.7519924.

[5] A. B. Soeth, P. R. F. de Souza, D. T. Custódio and I. Voloh, 'Traveling wave fault location on HVDC lines', in *2018 71st Annual Conference for Protective Relay Engineers (CPRE)*, 2018, pp. 1–16. DOI: 10.1109/CPRE.2018.8349832.

[6] A. E. Karlsen, 'Fault detection and location on HVDC transmission lines', in *Specialization Project, Department of Electric Power Engineering, Norwegian University of Science and Technology*, Dec. 2022.

[7] D. Jovcic, D. van Hertem, K. Linden, J.-P. Taisne and W. Grieshaber, 'Feasibility of DC Transmission Networks', in *2011 2nd IEEE PES International Conference and Exhibition on Innovative Smart Grid Technologies*, 2011, pp. 1–8. DOI: 10.1109/ISGTEurope.2011.6162829.

[8] A. Nami, J. Liang, F. Dijkhuizen and G. D. Demetriades, 'Modular Multilevel Converters for HVDC Applications: Review on Converter Cells and Functionalities', *IEEE Transactions on Power Electronics*, vol. 30, no. 1, pp. 18–36, 2015. DOI: 10.1109/TPEL.2014.2327641.

[9] M. P. Bahrman and B. K. Johnson, 'The ABCs of HVDC transmission technologies', *IEEE Power and Energy Magazine*, vol. 5, no. 2, pp. 32–44, 2007. DOI: 10.1109/MPAE.2007.329194.

[10] V. K. Sood, 'HVDC and FACTS Controllers: Applications of Static Converters in Power Systems', Springer, 2004. DOI: 10.1007/b117759.

[11] O. E. Oni, I. E. Davidson and K. N. Mbangula, 'A review of LCC-HVDC and VSC-HVDC technologies and applications', in *2016 IEEE 16th International Conference on Environment and Electrical Engineering (EEEIC)*, 2016, pp. 1–7. DOI: 10.1109/EEEIC.2016.7555677.

[12] Y. Jiang-Hafner, H. Duchen, M. Karlsson, L. Ronstrom and B. Abrahamsson, 'HVDC with Voltage Source Converters - A Powerful Standby Black Start Facility', in *2008 IEEE/PES Transmission and Distribution Conference and Exposition*, 2008, pp. 1–9. DOI: 10.1109/TDC.2008.4517039.

[13] B. Chuco and E. H. Watanabe, 'A comparative study of dynamic performance of HVDC system based on conventional VSC and MMC-VSC', in *2010 IREP Symposium Bulk Power System Dynamics and Control - VIII (IREP)*, 2010, pp. 1–6. DOI: 10.1109/IREP.2010.5563252.

[14] H. Saad, Y. Fillion, S. Deschanvres, Y. Vernay and S. Dennetière, 'On Resonances and Harmonics in HVDC-MMC Station Connected to AC Grid', *IEEE Transactions on Power Delivery*, vol. 32, no. 3, pp. 1565–1573, 2017. DOI: 10.1109/TPWRD.2017.2648887.

[15] A. Antonopoulos, L. Angquist and H.-P. Nee, 'On Dynamics and Voltage Control of the Modular Multilevel Converter', in *2009 13th European Conference on Power Electronics and Applications*, 2009, pp. 1–10.

[16] M. Davies, M. Dommaschk, J. Dorn, J. Lang, D. Retzmann Prof. Dr.-Ing and D. Soerangr, 'HVDC PLUS-basics and principle of operation', *Siemens Ag*, pp. 1–24, Jan. 2011.

[17] P. M. Meshram and V. B. Borghate, 'A Simplified Nearest Level Control (NLC) Voltage Balancing Method for Modular Multilevel Converter (MMC)', *IEEE Transactions on Power Electronics*, vol. 30, no. 1, pp. 450–462, 2015. DOI: 10.1109/TPEL.2014.2317705.

[18] M. Zygmanowski, B. Grzesik and R. Nalepa, 'Capacitance and Inductance Selection of the Modular Multilevel Converter', in *2013 15th European Conference on Power Electronics and Applications (EPE)*, 2013, pp. 1–10. DOI: 10.1109/EPE.2013.6634446.

[19] N. Raju, S. Jinkala, R. Mandi and M. ks, 'Modular multilevel converters technology: A comprehensive study on its topologies, modelling, control and applications', *IET Power Electronics*, vol. 12, Feb. 2019. DOI: 10.1049/iet-pel.2018.5734.

[20] Y. Li, X. Shi, B. Liu, F. Wang and W. Lei, 'Maximum Modulation Index for Modular Multilevel Converter with Circulating Current Control', in *2014 IEEE Energy Conversion Congress and Exposition (ECCE)*, 2014, pp. 491–498. DOI: 10.1109/ECCE.2014.6953434.

[21] Q. Tu, Z. Xu, H. Huang and J. Zhang, 'Parameter Design Principle of the Arm Inductor in Modular Multilevel Converter based HVDC', in *2010 International Conference on Power System Technology*, 2010, pp. 1–6. DOI: 10.1109/POWERCON.2010.5666416.

[22] J. Kang, D.-W. Kang, J.-P. Lee, D. W. Yoo and J. W. Shim, 'Design Procedure of MMC-HVDC System: Comprehensive Consideration of Internal and External Dynamics', *IEEE Access*, vol. 8, pp. 157 437–157 450, 2020. DOI: 10.1109/ACCESS.2020.3018597.

[23] M. Guan, Z. Xu and H. Chen, 'Control and Modulation Strategies for Modular Multilevel Converter based HVDC System', in *IECON 2011 - 37th Annual Conference of the IEEE Industrial Electronics Society*, 2011, pp. 849–854. DOI: 10.1109/IECON.2011.6119421.

[24] H. Saad, J. Peralta, S. Dennetière *et al.*, 'Dynamic Averaged and Simplified Models for MMC-Based HVDC Transmission Systems', *IEEE Transactions on Power Delivery*, vol. 28, no. 3, pp. 1723–1730, 2013. DOI: 10.1109/TPWRD.2013.2251912.

[25] W. Li, L.-A. Gregoire and J. Bélanger, 'Control and Performance of a Modular Multilevel Converter System', *CIGRÉ Canada, Conference on Power Systems, Halifax*, Jan. 2011.

[26] B. working group, 'Guide for the Development of Models for HVDC Converters in a HVDC Grid', *CIGRE technical report*, Dec. 2014.

[27] ENTSO-E, 'HVDC Links in System Operations', 2019.

[28] C. J. O'Rourke, M. M. Qasim, M. R. Overlin and J. L. Kirtley, 'A Geometric Interpretation of Reference Frames and Transformations: Dq0, Clarke, and Park', *IEEE Transactions on Energy Conversion*, vol. 34, no. 4, pp. 2070–2083, 2019. DOI: 10.1109/TEC.2019.2941175.

[29] A. U. Lawan, H. A. F. Almurib, J. G. Khor and S. Babani, 'Circulating Current control of a Modular Multilevel Converter (MMC) with State Feedback Controller and Harmonic Current Suppression', in *2018 IEEE International Conference on Electrical Systems for Aircraft, Railway, Ship Propulsion and Road Vehicles International Transportation Electrification Conference (ESARS-ITEC)*, 2018, pp. 1–8. DOI: 10.1109/ESARS-ITEC.2018.8607268.

[30] N. B. Kadandani, M. Dahidah and S. Ethni, 'Review of Circulating Current Control Methods in Modular Multilevel Converter', *Bayero Journal of Engineering and Technology (BJET)*, vol. 16, no. 1, pp. 62–75, 2021, ISSN: 2449–0539.

[31] N. ThinhQuach, S. Chae, S. Lee, H.-C. Kim and E.-H. Kim, 'Analyzing Modulation Techniques for the Modular Multilevel Converter', *International Journal of Computer and Electrical Engineering*, vol. 8, pp. 259–271, Jan. 2016. DOI: 10.17706/IJCEE.2016.8.4.259-271.

[32] Q. Tu, Z. Xu and L. Xu, 'Reduced Switching-Frequency Modulation and Circulating Current Suppression for Modular Multilevel Converters', *IEEE Transactions on Power Delivery*, vol. 26, no. 3, pp. 2009–2017, 2011. DOI: 10.1109/TPWRD.2011.2115258.

[33] E. Kontos, R. T. Pinto, S. Rodrigues and P. Bauer, 'Impact of HVDC Transmission System Topology on Multiterminal DC Network Faults', *IEEE Transactions on Power Delivery*, vol. 30, no. 2, pp. 844–852, 2015. DOI: 10.1109/TPWRD.2014.2357056.

[34] M. Marzinotto, G. Mazzanti and M. Nervi, 'Ground/sea return with electrode systems for HVDC transmission', *International Journal of Electrical Power & Energy Systems*, vol. 100, pp. 222–230, 2018, ISSN: 0142-0615. DOI: 10.1016/j.ijepes.2018.02.011.

[35] E. Deck, 'Types of HVDC Systems or Links - Monopolar, Bipolar & Homopolar links', 2021, Accessed: 2022-12-1 from https://www.electricaldeck.com/2021/08/types-of-hvdc-systems-or-links.html.

[36] A. Kalair, N. Abas and N. Khan, 'Comparative study of HVAC and HVDC transmission systems', *Renewable and Sustainable Energy Reviews*, vol. 59, pp. 1653–1675, 2016. DOI: 10.1016/j.rser.2015.12.288.

[37] D. Tzelepis, V. Psaras, E. Tsotsopoulou *et al.*, 'Voltage and Current Measuring Technologies for High Voltage Direct Current Supergrids: A Technology Review Identifying the Options for Protection, Fault Location and Automation Applications', *IEEE Access*, vol. 8, pp. 203 398–203 428, 2020. DOI: 10.1109/ACCESS.2020.3035905.

[38] J. R. Lucas, *High Voltage Engineering*. 2001, ch. High Voltage Cables, pp. 64–90.

[39] B. Li, W. Wang, B. Li, Y. Liu, W. Wen and X. Chen, 'Research on a current calculation method and characteristics of pole-to-ground faults in true bipolar MMC-HVDC grids considering line coupling', *Electric Power Systems Research*, vol. 192, p. 106 985, 2021, ISSN: 0378-7796. DOI: https://doi.org/10.1016/j.epsr.2020.106985.

[40] M. Muniappan, 'A comprehensive review of DC fault protection methods in HVDC transmission systems', in *Protection and Control of Modern Power Systems*, vol. 6, 2021. DOI: 10.1186/s41601-020-00173-9.

[41] A. S. Zalhaf, E. Zhao, Y. Han, P. Yang, A. H. Almaliki and R. M. H. Aly, 'Evaluation of the Transient Overvoltages of HVDC Transmission Lines Caused by Lightning Strikes', *Energies*, vol. 15, no. 4, 2022, ISSN: 1996-1073. DOI: 10.3390/en15041452.

[42] H.-C. Shu, G.-B. Zhang, Z.-Z. Zhu and S.-Q. Zhu, 'Modeling and Simulation of Lightning Electromagnetic Transient and Identification of Shielding Failure and Back Striking in ±800kV UHVDC Transmission Lines - Part I: Modeling and simulation of lightning electromagnetic transient', in *2009 Asia-Pacific Power and Energy Engineering Conference*, 2009, pp. 1–4. DOI: 10.1109/APPEEC.2009.4918495.

[43] H. K. Hoidalen, 'TET4130 Overspenninger', 2020, Accessed 2022-12-13 from the subject TET4130 Overspenninger Course on Blackboard.

[44] E. O. Schweitzer, A. Guzmán, M. V. Mynam, V. Skendzic, B. Kasztenny and S. Marx, 'Locating faults by the traveling waves they launch', in *2014 67th Annual Conference for Protective Relay Engineers*, 2014, pp. 95–110. DOI: 10.1109/CPRE.2014.6798997.

[45] 3. working group, 'Overvoltages on HVDC Cables: Final Report', *CIGRE*, Aug. 1994.

[46] 'IEEE Standard for High-Voltage Testing Techniques', *IEEE Std. 4-2013*, May 2013.

[47] M. Goertz, S. Wenig, S. Gorges *et al.*, 'Lightning Overvoltages in a HVDC Transmission System comprising Mixed Overhead-Cable Lines', Jun. 2017.

[48] Z. Xu, H. Xiao, L. Xiao and Z. Zhang, 'DC Fault Analysis and Clearance Solutions of MMC-HVDC Systems', vol. 11, no. 4, 2018. DOI: 10.3390/en11040941.

[49] F. Mohammadi, K. Rouzbehi, M. Hajian *et al.*, 'HVDC Circuit Breakers: A Comprehensive Review', *IEEE Transactions on Power Electronics*, vol. 36, no. 12, pp. 13 726–13 739, 2021. DOI: 10.1109/TPEL.2021.3073895.

[50] X. Li, Q. Song, W. Liu, H. Rao, S. Xu and L. Li, 'Protection of Nonpermanent Faults on DC Overhead Lines in MMC-Based HVDC Systems', *IEEE Transactions on Power Delivery*, vol. 28, no. 1, pp. 483–490, 2013. DOI: 10.1109/TPWRD.2012.2226249.

[51] A. Grid, *Network Protection & Automation Guide: Protective Relays, Measurement & Control.* Alstom Grid, 2011, ISBN: 978-0-9568678-0-3.

[52] ENTSO-E, 'Use of travelling waves principle in protection systems and related automations', 2021.

[53] C. Zhang, G. Song, T. Wang and L. Yang, 'Single-Ended Traveling Wave Fault Location Method in DC Transmission Line Based on Wave Front Information', *IEEE Transactions on Power Delivery*, vol. 34, no. 5, pp. 2028–2038, 2019. DOI: 10.1109/TPWRD.2019.2922654.

[54] C. M. S. Ribeiro, F. V. Lopes and K. M. e Silva, 'Assessment of Traveling Wave Propagation Velocity on HVDC Transmission Lines', in *2022 Workshop on Communication Networks and Power Systems (WCNPS)*, 2022, pp. 1–6. DOI: 10.1109/WCNPS56355.2022.9969692.

[55] Y. N. Velaga, K. Prabakar, A. Singh and P. K. Sen, 'Traveling Wave Relays for Distribution Feeder Protection with High Penetrations of Distributed Energy Resources', in *2021 IEEE Rural Electric Power Conference (REPC)*, 2021, pp. 59–66. DOI: 10.1109/REPC48665.2021.00016.

[56] D. Naidoo and N. Ijumba, 'HVDC line protection for the proposed future HVDC systems', in *2004 International Conference on Power System Technology, 2004. PowerCon 2004.*, vol. 2, 2004, 1327–1332 Vol.2. DOI: 10.1109/ICPST.2004.1460207.

[57] B. J. Cory and P. F. Gale, 'Satellites for power system applications', *Power Engineering Journal*, vol. 7, no. 5, pp. 201–207, 1993. DOI: 10.1049/pe:19930050.

[58] J. Machowski, Z. Lubosny, J. W. Bialek and J. R. Bumby, *Power System Dynamics: Stability and Control.* John Wiley & Sons, 2020, ch. Wide-Area Monitoring and Control, pp. 709–733, 3rd edition.

[59] *Protection requirements on transient response of digital acquisition chain.* Paris: CIGRE, 2019.

[60] J. Schmid and K. Kunde, 'Application of Non Conventional Voltage and Currents Sensors in High Voltage Transmission and Distribution Systems', in *2011 IEEE International Conference on Smart Measurements of Future Grids (SMFG) Proceedings*, 2011, pp. 64–68. DOI: 10.1109/SMFG.2011.6125766.

[61] 'Power Engineering Guide Edition 8.0', 2017, Accessed 2023-3-15 from: https://assets.new.siemens.com/siemens/assets/api/uuid:5bfb815b0db95760272f17c1329cc56c0c402686/peg8-final-160812.pdf.

[62] J. Ramboz, 'Machinable Rogowski Coil, Design, and Calibration', *IEEE Transactions on Instrumentation and Measurement*, vol. 45, no. 2, pp. 511–515, 1996. DOI: 10.1109/19.492777.

[63] D. M. d. Silva, F. B. Costa, V. Miranda and H. Leite, 'Wavelet-based analysis and detection of traveling waves due to DC faults in LCC HVDC systems', *International Journal of Electrical Power & Energy Systems*, vol. 104, pp. 291–300, 2019, ISSN: 0142-0615. DOI: https://doi.org/10.1016/j.ijepes.2018.07.011.

[64]   M. Fundamentals, 'A guide for using the Wavelet Transform in Machine Learning', Accessed: 2023-4-5 from https://ataspinar.com/2018/12/21/a-guide-for-using-the-wavelet-transform-in-machine-learning/.

[65]   R. Singh, S. Nigam, A. K. Singh and M. Elhoseny, *Intelligent Wavelet Based Techniques for Advanced Multimedia Applications*, en. Cham: Springer International Publishing, 2020, ISBN: 978-3-030-31872-7. DOI: 10.1007/978-3-030-31873-4. [Online]. Available: http://link.springer.com/10.1007/978-3-030-31873-4.

[66]   F. Magnago and A. Abur, 'Fault location using wavelets', *IEEE Transactions on Power Delivery*, vol. 13, no. 4, pp. 1475–1480, 1998. DOI: 10.1109/61.714808.

[67]   J.-P. Antoine, P. Carrette, R. Murenzi and B. Piette, 'Image analysis with two-dimensional continuous wavelet transform', *Signal Processing*, vol. 31, pp. 241–272, 1993. DOI: 10.1016/0165-1684(93)90085-O.

[68]   A. Borghetti, S. Corsi, C. A. Nucci, M. Paolone, L. Peretto and R. Tinarelli, 'On the use of continuous-wavelet transform for fault location in distribution power systems', *International Journal of Electrical Power & Energy Systems*, vol. 28, no. 9, pp. 608–617, 2006, ISSN: 0142-0615. DOI: https://doi.org/10.1016/j.ijepes.2006.03.001.

[69]   M. Abdul Baseer, P. R.P., A. Abo-Khalil, E. M. Barhoumi and Y. Berrouche, 'Localisation of Fault Using Travelling Wave Theory Based on Multi-End System', *International Journal of Applied Engineering Research*, vol. 12, pp. 6504–6513, 2017, ISSN: 0973-4562.

[70]   K. Nanayakkara, A. Rajapakse and R. Wachal, 'Fault Location in Extra Long HVDC Transmission Lines using Continuous Wavelet Transform', *International Conference on Power Systems Transients*, 2011.

[71]   MathWorks, 'Choose a Wavelet', Accessed 2023-4-5 from: https://www.mathworks.com/help/wavelet/gs/choose-a-wavelet.html.

[72]   F. Xie, A. Haddad and H. Griffiths, 'Single-Ended Fault Location Method Based on Wavelet Theory: Application to a Double-Circuit Transmission Line', in *2013 48th International Universities' Power Engineering Conference (UPEC)*, 2013, pp. 1–6. DOI: 10.1109/UPEC.2013.6714862.

[73]   W. Fluty and Y. Liao, 'Electric Transmission Fault Location Techniques Using Traveling Wave Method and Discrete Wavelet Transform', in *2020 Clemson University Power Systems Conference (PSC)*, 2020, pp. 1–8. DOI: 10.1109/PSC50246.2020.9131271.

[74]   FBN/AIE, 'Requirements - HVDC, Rev. 0', 2019.

[75]   G. Ma, L. Jiang, K. Zhou and G. Xu, 'A Method of Line Fault Location Based on Traveling Wave Theory', in *International Journal of Control nd Automation*, vol. 9, 2016, pp. 261–270. DOI: 10.14257/ijca.2016.9.2.25.

[76]   O. Altay, E. Gursoy and O. Kalenderli, 'Single End Travelling Wave Fault Location on Transmission Systems Using Wavelet Analysis', in *2014 ICHVE International Conference on High Voltage Engineering and Application*, 2014, pp. 1–4. DOI: 10.1109/ICHVE.2014.7035486.

[77] PSCAD, 'Modular Multi-Level Converter (MMC)', Accessed 2023-1-20 from: https://www.pscad.com/knowledge-base/article/234.

[78] K. Nanayakkara and A. Rajapakse, 'Location of DC Line Faults in Conventional HVDC Systems with Segments of Cables and Overhead Lines Using Terminal Measurements', in *2012 IEEE Power and Energy Society General Meeting*, 2012, pp. 1–1. DOI: 10.1109/PESGM.2012.6343919.

[79] J. Ding, L. Li, Y. Zheng, C. Zhao, H. Chen and X. Wang, 'Distribution travelling-wave-based fault location without time synchronisation and wave velocity error', *IET Generation, Transmission & Distribution*, vol. 11, no. 8, pp. 2085–2093, 2017. DOI: 10.1049/iet-gtd.2016.1778.

[80] P. K. Murthy, J. Amarnath, S. Kamakshiah and B. Singh, 'Wavelet Transform Approach for Detection and Location of Faults in HVDC System', in *2008 IEEE Region 10 and the Third international Conference on Industrial and Information Systems*, 2008, pp. 1–6. DOI: 10.1109/ICIINFS.2008.4798483.

[81] GE, 'About us: GE Mission Statement & Values', Accessed 2023-3-14 from: https://www.ge.com/about-us.

[82] GE, 'Reason RPV311', Accessed 2023-3-14 from: https://www.gegridsolutions.com/products/brochures/reason%20rpv311-brochure-en-2018-05-33113-a4.pdf.

[83] KEHUI, 'KEHUI - THE APPLICATION OF TECHNOLOGY', Accessed 2023-3-14 from: https://www.kehui.com/#.

[84] KEHUI, 'XC-2100E TRAVELLING WAVE FAULT LOCATION SYSTEM', Accessed 2023-3-14 from: https://kehui.wpenginepowered.com/wp-content/uploads/2023/01/XC-2100E_BR_1222_LR.pdf.

[85] M. H. R. Centre, 'EMTDC Transient Analysis for PSCAD Power System Simulation', 2010, Version 4.7, fifth printing.

[86] J. Bremnes and G. Evenset, 'Frequency dependency of single-core cable parameters', *9th International Conference on Insulated Power Cables*, 2015.

Appendix A

PSCAD: HVDC-MMC model parameters

In this section, the parameters used for the modeling of the HVDC-MMC system are given. This includes the MMC system and the different transmission line segments.

A.1 General system parameters

Table A.1 gives the parameters of the overall system and system control different from the example model.

Table A.1: System parameters

General	
Frequency	50
Number of sub-modules	115
Number of levels PWM	116
Norway AC grid	
Voltage source	$420\,\mathrm{kV}$
Source impedance type	Resistive $(1\,\Omega)$
Rated power	$700\,\mathrm{MW}$
Rated DC voltage	$515\,\mathrm{kV}$
Active power increase/decrease rates	$800\frac{\mathrm{MW}}{\mathrm{s}}$
Transformer ratio (grid/VSC)	$415\,\mathrm{kV}/337\,\mathrm{kV}$
MMC (rectifier and inverter)	
Cell DC capacitor	$3900\,\mathrm{\mu F}$
Arm reactor	$80\,\mathrm{mH}$
Rated AC voltage	$337\,\mathrm{kV}$
Rated MVA	$700\,\mathrm{MV\,A}$
Controls Terminal 1 and 2	
VdcRef1	515
Pref2/pole	-700
Transmission lines	
Overhead line length	$53\,\mathrm{km}$
Sub-sea cable length	$516\,\mathrm{km}$
Chopper	
Enable (1) or Disable (0)	1
Power	$700\,\mathrm{MW}$
Base DC link voltage	$515\,\mathrm{kV}$
Germany AC grid	
Voltage source	$380\,\mathrm{kV}$
Source impedance type	Resistive $(1\,\Omega)$
Rated power	$700\,\mathrm{MW}$
Rated DC voltage	$515\,\mathrm{kV}$
Active power increase/decrease rates	$800\frac{\mathrm{MW}}{\mathrm{s}}$
Vdc set point	515
Transformer ratio (grid/VSC)	$375\,\mathrm{kV}/337\,\mathrm{kV}$

A.2   Cable and overhead line parameters

Table A.2: Sub-sea cable parameters

Core Conductor Data	
Resistivity	$1.68 \times 10^{-8}\,\Omega\,\mathrm{m}$
Relative permeability	1.0
Outer radius	$0.023\,\mathrm{m}$
1st Insulating and Semi-Conductor Layer Data	
Semi-conducting layers	Present
Relative permittivity	4.2
Relative permeability	1.0
Outer radius	$0.043\,\mathrm{m}$
Inner semi-conducting layer thickness	$0.001\,\mathrm{m}$
Outer semi-conducting layer thickness	$0.001\,\mathrm{m}$
1st Conducting Layer Data	
Resistivity	$2.2 \times 10^{-7}\,\Omega\,\mathrm{m}$
Relative permeability	1.0
Outer radius	$0.0465\,\mathrm{m}$
2nd Insulating Layer Data	
Relative permittivity	2.3
Relative permeability	1.0
Outer radius	$0.050\,\mathrm{m}$
2nd Conducting Layer Data	
Resistivity	$1.8 \times 10^{-7}\,\Omega\,\mathrm{m}$
Relative permeability	400.0
Outer radius	$0.0608\,\mathrm{m}$
3rd Insulating Layer Data	
Relative permittivity	1.0
Relative permeability	1.0
Outer radius	$0.066\,\mathrm{m}$

Table A.3: Overhead line parameters

Conductor Data	
Conductor style	Hollow
Outer radius	$0.019\,15\,\mathrm{m}$
Inner radius	$0.0064\,\mathrm{m}$
DC resistance	$0.0377\frac{\Omega}{\mathrm{km}}$
Sag	$5\,\mathrm{m}$
Bundled sub-conductors	3
Bundle configuration	Symmetrical
Sub-conductor spacing	$0.45\,\mathrm{m}$
Ground Wire Data	
Ground wire elimination	Disabled
Sag	$5\,\mathrm{m}$
Outer radius	$0.0105\,\mathrm{m}$
DC resistance	$0.28\frac{\Omega}{\mathrm{km}}$

PSCAD: DC voltage source model

The simplified DC voltage source model used for comparison with the MMC model is given here. The overhead line and the cable are modeled the same way as in the HVDC-MMC model. Two DC voltage sources are attached on each side of the system. The DC sources marked in red give negative voltages of $515\,$kV. As it is more difficult to control the system parameters, the resistances on the end of the sub-sea cable is $800\,\Omega$ on each pole, to approximately match the DC currents flowing in the other model.
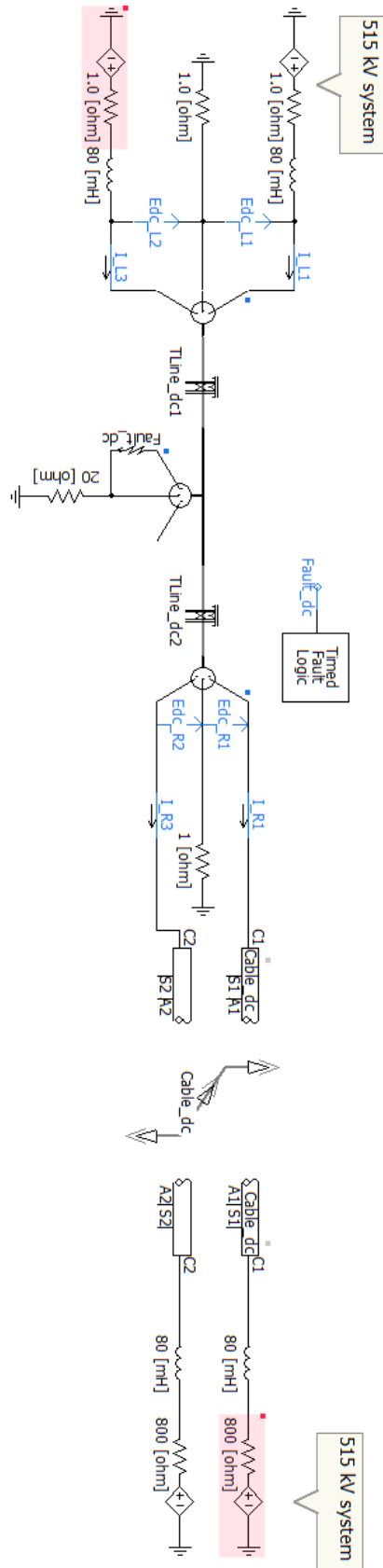
Figure B.1: Simple DC voltage source model

C

Appendix

MATLAB fault locator algorithm

The TWFL algorithms consist in total of 4 functions. One function is specifically for the double-ended method and one is for the single-ended method. The two other function are used for both single-ended and double ended method. These are functions for doing the Haar wavelet transformation and for finding the peaks of the detail coefficients.

```matlab
%% Haar wavelet transformation, level 1
function detail_coef = haar_transform(signal)
    [c,l] = wavedec(signal, 1, 'haar');
    detail_coef = detcoef(c,l,1); %Obtaining detail coefficient
end

%% Detail coefficient peak estimation
function TW_sampling_sorted = peak_estimation(coefficient)
    threshold = 10;   %Threshold for peak detection
    [peak,location] = findpeaks(coefficient); %All positive peaks
        from signal
    [peak_neg,location_neg] = findpeaks(-coefficient); %All
        negative peaks from signal
    TW_pos = [];
    TW_neg = [];

    for i = 1:length(peak)
        if peak(i) > threshold %Comparing to peak threshold
            TW_pos = [TW_pos, location(i)];
        end
    end
    for i = 1:length(peak_neg)
        if peak_neg(i) > threshold %Comparing to peak threshold
            TW_neg = [TW_neg, location_neg(i)];
```

```matlab
            end
        end


        %Sorting peaks after location
        if length(TW_pos) > 0
            if length(TW_neg) > 0
                TW_sampling = [TW_pos(1),TW_neg(1)];
                TW_sampling_sorted = sort(TW_sampling);
            else
                TW_sampling = TW_pos;
                TW_sampling_sorted = TW_sampling;
            end
        else
            TW_sampling = TW_neg;
            TW_sampling_sorted = TW_sampling;
        end
end

%% Double-ended TWFL algorithm
function double_endedTWFL(voltageL,voltageR)
    l_line = 53; %line length
    v = 294444.444; %wave velocity

    detail_coefL = haar_transform(voltageL);
    detail_coefR = haar_transform(voltageR);
    TW_sampling_sortedL = peak_estimation(detail_coefL);
    TW_sampling_sortedR = peak_estimation(detail_coefR);

    if (isempty(peak_estimation(detail_coefL))) || (isempty(
       peak_estimation(detail_coefR)))
        fprintf('No fault located.\n')
        return %Ending function if no fault
    end
    %Obatining time locations, input signal 0.1 sec
    t_L = TW_sampling_sortedL(1)/(length(detail_coefL)*10);
    t_R = TW_sampling_sortedR(1)/(length(detail_coefR)*10);
    %Calculating fault location
    loc_L = (l_line - v*(t_R-t_L))/2;
    loc_R = (l_line + v*(t_R-t_L))/2;
    fprintf('Fault is located %.3f km from terminal L and %.3f km
        from terminal R.\n', m, n)
end
```

```matlab
%% Single-ended TWFL algorithm
function single_endedTWFL(voltageL)
    l_line = 53; %line length
    v = 294444.444; %wave velocity

    detail_coef = haar_transform(voltageL);
    TW_sampling_sorted = peak_estimation(detail_coef);

    if isempty(peak_estimation(detail_coef))
        fprintf('No fault located.\n')
    elseif length(TW_sampling_sorted) < 2
        fprintf('No fault located.\n')
    else
        %Determine location of fault
        if abs(detail_coef(TW_sampling_sorted(2)))<50
            fault = 2; %fault located on second half
        else
            fault = 1; %fault located on first half
        end
        %Obatining time locations, input signal 0.1 sec
        t1 = TW_sampling_sorted(1)/(length(detail_coef)*10);
        t2 = TW_sampling_sorted(2)/(length(detail_coef)*10);
        %Calculating fault location
        if fault == 1
            loc_L = v*(t2-t1)/2;
            fprintf('Fault is located %.3f from terminal L.\n',m)
        elseif fault == 2
            loc_L = l_line - (v*(t2-t1)/2);
            fprintf('Fault is located %.3f from terminal L.\n',m)
        else
            fprintf('No fault located.\n')
        end
    end
end
```

D
Appendix

Results

D.1 Fault position variation

Table D.1: Peak values of different fault positions

Test number	Fault position [km]	First peak L	Second peak L	First peak R
1	2.65	320.9	-193.7	48.0
2	7.95	229.1	-146.9	19.4
3	18.55	77.3	-76.8	34.3
4	26.5	260.4	-50.0	42.1
5	34.45	204.9	-27.8	15.2
6	45.05	107.8	-20.5	39.2
7	50.35	296.0	1.83	51.4

D.2 Fault resistance variation

Table D.2: Peak values of different fault resistances for different positions

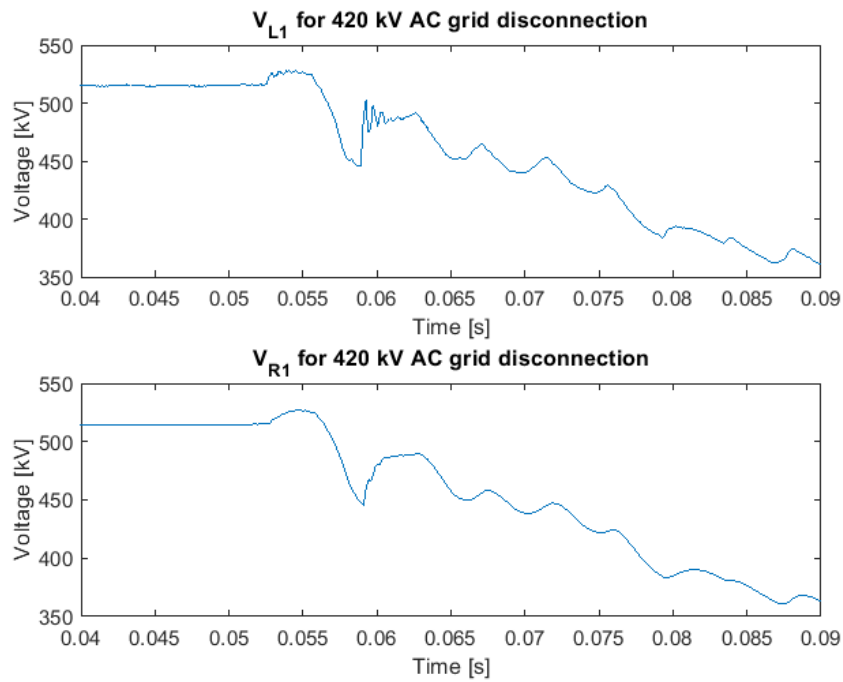| Fault position [km]	Resistance [Ω]	First peak L	Second peak L	First peak R
	0.1	77.3	-76.8	34.3
18.55	10.0	73.5	-69.9	32.6
	100	50.8	-35.8	22.2
	0.1	260.36	-50.0	42.1
26.5	10.0	246.8	-47.3	39.9
	100	167.5	-31.9	27.1
	0.1	204.9	-27.8	15.2
34.45	10.0	194.3	-30.0	14.7
	100	132.3	-35.0	9.96

D.3   AC grid disconnection

Figure D.1: Voltage responses at each terminal for AC grid disconnection
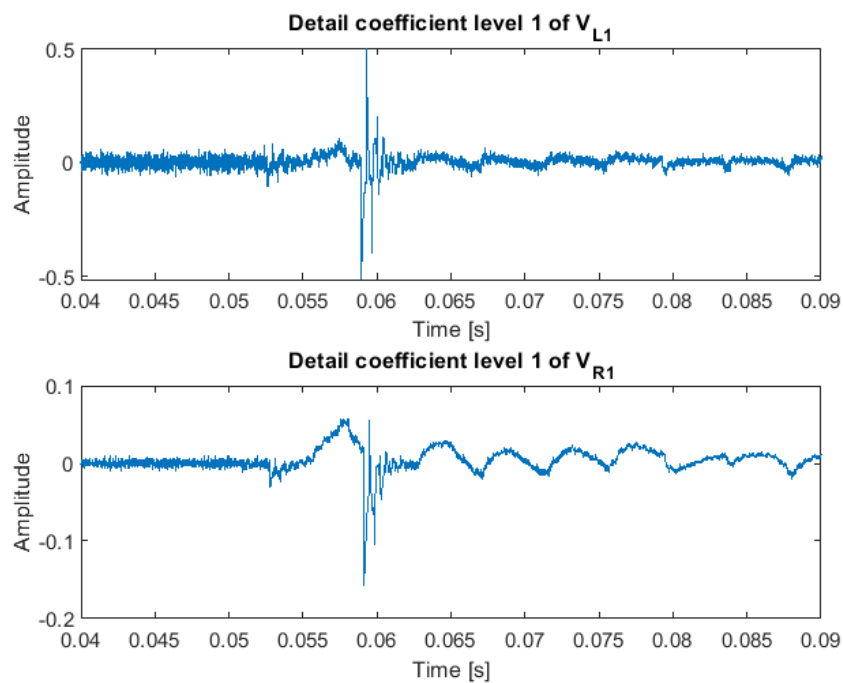

Figure D.2: Detail coefficients at each terminal for AC grid disconnection

D.4 MMC VS. DC voltage source model

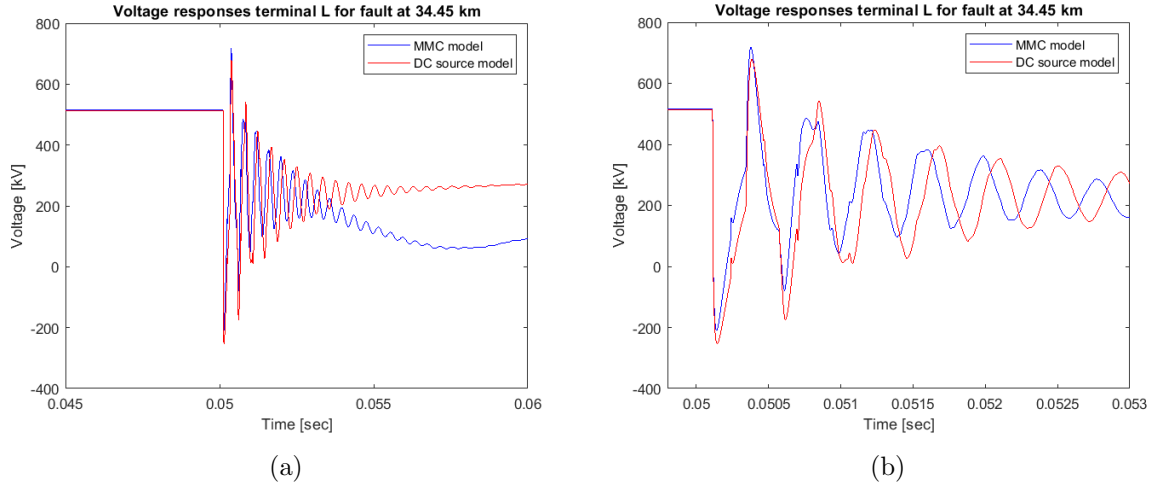### D.4.1 Voltage responses and detail coefficients for fault at 34.45 km

Figure D.3: Voltage responses at terminal L for HVDC-MMC model and DC voltage source model at fault position 34.45 km
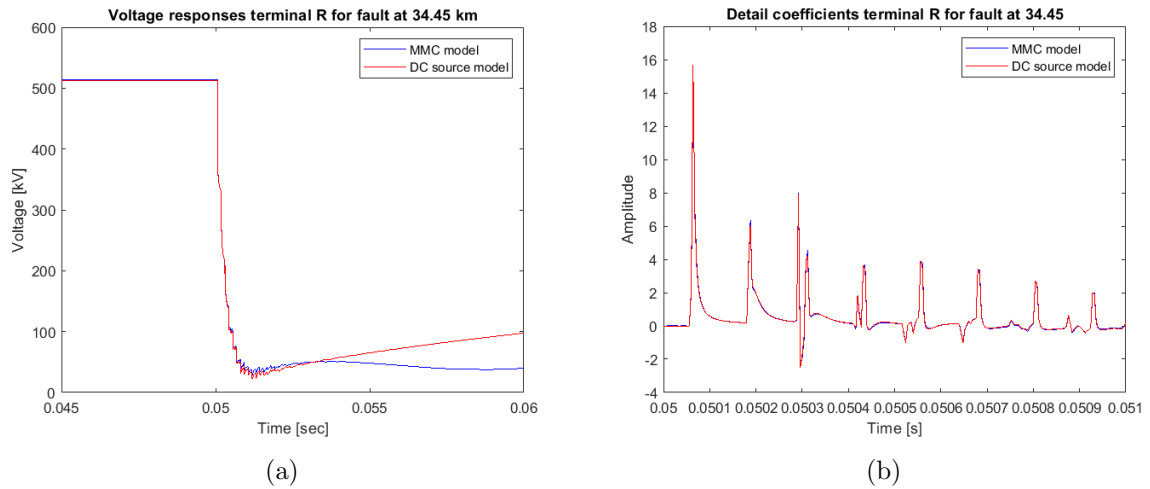

Figure D.4: Voltage responses at terminal R for HVDC-MMC model and DC voltage source model at fault position 34.45 km
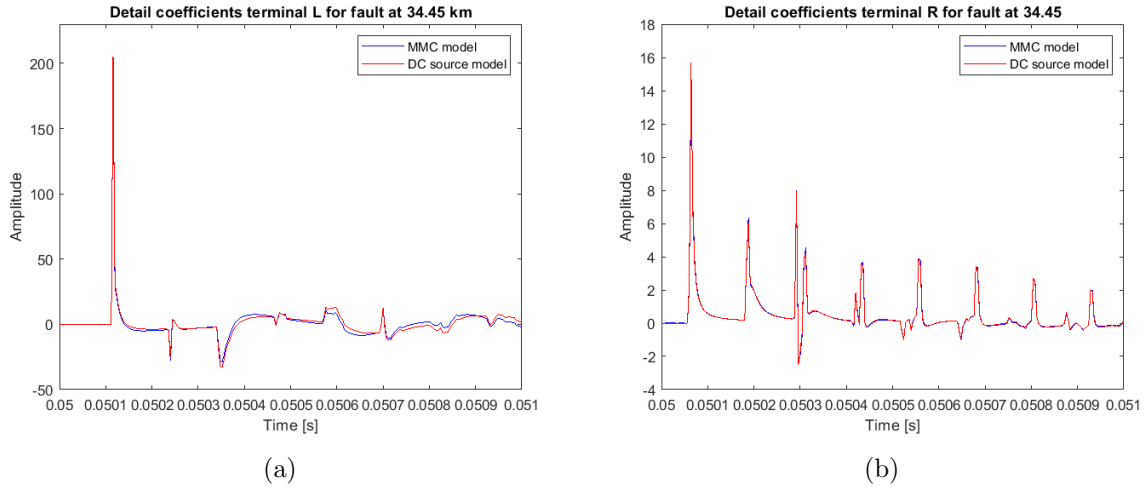
(a)   (b)

Figure D.5: Detail coefficients for HVDC-MMC model and DC voltage source model at fault position 34.45 km

D.4.2   Detail coefficient peak values of different modeling approaches

Table D.3: Peak values of the HVDC-MMC model and two sampling times of DC voltage source model with two different positions

Fault position [km]	Model	First peak L	Second peak L	First peak R
18.55	MMC (2 µs)	77.3	-76.8	34.3
	DC (2 µs)	82.5	-85.6	34.0
	DC (1 µs)	326.5	-48.5	9.01
34.45	MMC (2 µs)	204.9	-27.8	15.2
	DC (2 µs)	205.1	-25.7	15.7
	DC (1 µs)	46.0	-10.3	51.4